

Frontal Waves in the East of the Tsugaru Strait Revealed by the High-Frequency Radar Observation

Hitoshi KANEKO (✉ h_kaneko@jamstec.go.jp)

JAMSTEC: Kaiyo Kenkyu Kaihatsu Kiko <https://orcid.org/0000-0002-7937-2397>

Takahiro Tanaka

Japan Fisheries Research and Education Agency: Kokuritsu Kenkyu Kaihatsu Hojin Suisan Kenkyu Kyoiku Kiko

Hiroto Abe

Hokkaido University Faculty of Fisheries Sciences Graduate School of Fisheries Sciences School of Fisheries Sciences: Hokkaido Daigaku Daigakuin Suisan Kagaku Kenkyuin Daigakuin Suisan Kagakuin Suisan Gakubu

Masahide Wakita

JAMSTEC: Kaiyo Kenkyu Kaihatsu Kiko

Ken'ichi Sasaki

JAMSTEC: Kaiyo Kenkyu Kaihatsu Kiko

Takeshi Okunishi

Japan Fisheries Research and Education Agency: Kokuritsu Kenkyu Kaihatsu Hojin Suisan Kenkyu Kyoiku Kiko

Shuichi Watanabe

JAMSTEC: Kaiyo Kenkyu Kaihatsu Kiko

Shoko Tatamisashi

JAMSTEC: Kaiyo Kenkyu Kaihatsu Kiko

Yoshiaki Sato

JAMSTEC: Kaiyo Kenkyu Kaihatsu Kiko

Research article

Keywords: Tsugaru Strait, Tsugaru Warm Current, High frequency radar, Frontal waves, Tide, Baroclinic instability

Posted Date: June 29th, 2021

DOI: <https://doi.org/10.21203/rs.3.rs-629560/v1>

License:  This work is licensed under a Creative Commons Attribution 4.0 International License.

[Read Full License](#)

1 **Frontal waves in the east of the Tsugaru Strait revealed by**
2 **the high-frequency radar observation**

3 Hitoshi Kaneko¹

4 Corresponding author

5 Email: h_kaneko@jamstec.go.jp

6

7 Takahiro Tanaka²

8 Email: takahiro@affrc.go.jp

9

10 Hiroto Abe^{1,3}

11 Email: abe@fish.hokudai.ac.jp

12

13 Masahide Wakita¹

14 Email: mwakita@jamstec.go.jp

15

16 Ken'ichi Sasaki¹

17 Email: ksasaki@jamstec.go.jp

18

19 Takeshi Okunishi²

20 Email: okunishi@affrc.go.jp

21

22 Shuichi Watanabe¹

23 Email: swata@jamstec.go.jp

24

25 Shoko Tatamisashi¹

26 Email: tatamisashis@jamstec.go.jp

27

28 Yoshiaki Sato¹

29 Email: satoyoshi@jamstec.go.jp

30

31 (Institutional addresses)

32 ¹ Mutsu Institute for Oceanography, Research Institute for Global Change, Japan Agency for

33 Marine-Earth Science and Technology, 690 Kitasekine, Sekine, Mutsu, Aomori 035-0022,

34 Japan

35 ² Fisheries Resources Institute, Japan Fisheries Research and Education Agency, 3-27-5

36 Shinhama-cho, Shiogama, Miyagi 985-0001, Japan

37 ³ Faculty of Fisheries Sciences, Hokkaido University, 3-1-1 Minato-cho, Hakodate, Hokkaido,

38 041-8611, Japan

39

40 **Abstract**

41 Surface velocity observations of the eastern part of the Tsugaru Strait made by the high-
42 frequency radar revealed frequent occurrence of frontal waves along the axis of the Tsugaru
43 Warm Current in 2017–2019. The current axis (maximum of the zonal velocity in the meridional
44 direction) disturbed in the north–south direction with period of ~ 13.7 days that is dominant
45 timescale of tide modulation in the strait, in addition to that of ~ 27.3 days. The amplitude of the
46 axis fluctuation increased in the downstream direction, from the eastern neck of the channel
47 ($\sim 141.0^\circ\text{E}$) to the outlet of the strait adjacent to the Pacific Ocean ($\sim 141.5^\circ\text{E}$). The propagation
48 speed of the disturbance was slower than that due to surface advection especially in the seasons
49 when the stratification was developed, and agreed well with that estimated from the theory
50 based on the two-layer baroclinic instability model except for winter. The north–south
51 modulation of the axis at the outlet of the strait ($\sim 141.5^\circ\text{E}$) could cause short-term (from 20
52 days to 1 month) variations of an anticyclonic gyre of the Tsugaru Warm Current that is
53 developed in the east of the outlet from summer to autumn reported by the previous studies.

54

55 **Keywords**

56 Tsugaru Strait, Tsugaru Warm Current, High frequency radar, Frontal waves, Tide, Baroclinic
57 instability

58

59 **1 Introduction**

60 The Tsugaru Warm Current (TWC) is a remarkable flow in the Tsugaru Strait, between
61 the mainland of Japan and Hokkaido, from west to east (Fig. 1a). The origin of the TWC is the
62 Kuroshio which bifurcates in the south of the Kyushu Island, as well as the flow from the
63 Taiwan Strait (Isobe, 1999). The current called as the Tsushima Warm Current flows
64 northeastward along the mainland of Japan, and again the current bifurcates at the west of the
65 Tsugaru Strait into the strait (Fig. 1a). The other branch flows northward along the Hokkaido to
66 the Soya Strait (Fig. 1a). Kida et al. (2020) suggested that long-term trend of the volume
67 transport of the throughflow at the Tsushima Strait is deeply related with the trend of the latitude
68 of the eastward Kuroshio position. Thus, the variation of the TWC would be closely connected
69 with those of these flows including the Kuroshio and the Tsushima Warm Current as one flow
70 system (Kida et al., 2016; Kida et al., 2020).

71 In the Tsugaru Strait, recent studies reported significant disturbance due to the intense
72 flow and tides (e.g., Yamaguchi et al., 2020; Tanaka et al., 2021), and subsequent characteristic

73 change in ocean environment there (Wakita et al., 2021). Yamaguchi et al. (2020) suggested
74 generation of internal waves that have large-amplitude in the vertical direction behind a
75 characteristic topography (sill) in the western part of the strait based on observations and
76 numerical experiment. Around the sill where Yamaguchi et al. (2020) made the investigation,
77 Tanaka et al. (2021) observed far stronger turbulence than that in the open ocean (the turbulent
78 energy dissipation rate: $O(10^{-6}) \text{ W kg}^{-1}$, the vertical diffusive coefficient: $O(10^{-2}) \text{ m}^2 \text{ s}^{-1}$), and
79 estimated subsequent vertical transport of nitrate behind the sill ($1 \text{ mmol m}^{-2} \text{ day}^{-1}$). The value
80 is far larger than that observed by Kaneko et al. (2021) in the subarctic region of the Western
81 North Pacific during summer as $\sim 1 \times 10^{-2} \text{ mmol m}^{-2} \text{ day}^{-1}$. In addition, Wakita et al. (2021)
82 found faster acidification in the strait based on the recent observation (2012–2019; the decrease
83 rate of pH is $0.0030\text{--}0.0051 \text{ year}^{-1}$) than that in the open ocean ($0.0013\text{--}0.0024 \text{ year}^{-1}$; Dore et
84 al., 2009; Astor et al., 2013; Wakita et al., 2017; Ono et al., 2019). Moreover, Wagawa et al.
85 (2015) suggested that the volume transport of the TWC could affect the temperature in the
86 downstream coastal region, which have a big impact on aquacultures such as a kind of seaweed
87 (*Undaria pinnatifida*). Therefore, behaviors of the TWC in the strait would be subject to
88 investigate, because these characteristic phenomena in the strait could affect a wider region via
89 the TWC.

90 The mean velocity of the TWC in the strait reaches to 1 m s^{-1} at the axis of the current

91 (e.g., Ito et al. 2003; Matsuura et al., 2007; Saitoh et al., 2008). Its mean volume transport was
92 estimated as about 1.5 Sv ($10^6 \text{ m}^3 \text{ s}^{-1}$; Onishi and Ohtani, 1997; Ito et al., 2003) with seasonal
93 variability of about ~ 0.3 Sv, showing an increase from summer to autumn (Nishida et al., 2003).
94 The outflow from the channel encounters low temperature and salinity water described as the
95 coastal Oyashio water by the previous studies (e.g., Kono et al., 2004; Rosa et al., 2007; Saitoh
96 et al., 2008; Kuroda et al. 2012; Wakita et al., 2021) in the outlet of the eastern neck of the
97 channel ($\sim 141.2^\circ\text{E}$; Fig. 1b). Thus, steep front of water mass in the north–south direction can
98 occur in the east part of the strait (e.g., Matsuura et al., 2007; Saitoh et al. 2008; Kuroda et al.
99 2012), where the north boundary is open. More recent studies based on the surface velocity
100 observation obtained from the high-frequency radar (HFR) reported seasonal variation of the
101 latitude of the current axis; northward in summer and autumn, and shifts southward in winter and
102 spring (Abe et al., 2020; Yasui et al., submitted to Journal of Oceanography as “Seasonal
103 pathways of Tsugaru Warm Current revealed by high-frequency ocean radar”, hereafter Y21,
104 and Kaneko et al., submitted to GRL as “The role of an intense jet in the Tsugaru Strait in the
105 formation of the outflow gyre revealed using high-frequency radar data”, hereafter K21). The
106 outflow pattern in the east of the strait (east of $\sim 141.5^\circ\text{E}$) also changed drastically in summer
107 and autumn, that is, large anticyclonic gyre develops south of Hokkaido (e.g., Conlon, 1982;
108 Kawasaki and Sugimoto, 1984; Kubokawa, 1991; Rosa et al. 2007; K21).

109 In addition to these seasonal changes, shorter variation of TWC was also reported.
110 Whereas the growth of the gyre takes for about 3 months (Yasuda et al., 1988; Nof and Pichevin,
111 2001), Yasuda et al. (1988) reported shorter-term variation of the gyre that has 20–30 days
112 period, that is, the direction of the major axis of the elliptical distortion of the gyre rotated
113 clockwise with these fluctuations. As another short-term variation in the strait, based on a
114 mooring observation for about a year located at the southeastern corner of the channel (41.77°N,
115 141.12°E), Tanno et al. (2005) reported existence of remarkable periodic variation of the surface
116 current with about 13.66 days period in addition to the four major tidal constituents (M2, S2,
117 K1, and O1). They concluded that the variation of 13.66 days would be related with Mf tide,
118 that is dominant timescale in the strait (e.g., Onishi et al., 2004) as well as in the Soya Strait
119 (Ebuchi et al., 2009), and/or spring–neap tide for K1 and O1 constituents. Based on a numerical
120 model, Kubokawa (1991) demonstrated that variation of the north–south position of the front
121 at the outlet of the strait could affect rotation of the gyre in a clockwise direction that is resemble
122 with the short-term variation reported by Yasuda et al. (1988), however, the connection of such
123 short-term variation of the gyre and tides are not fully understood, yet.

124 Since remarkable front of the water mass and periodical disturbance due to tide are
125 known in the strait as mentioned above, frontal disturbance related with the tide would be likely
126 to occur in the east part of the strait (from ~141.0 to ~141.6°E, Fig. 1b). Frontal waves that are

127 propagating meander along remarkable front to the downstream direction were reported in other
128 regions including the Kuroshio in the East China Sea (Sugimoto et al., 1988; Qiu et al., 1990;
129 James et al., 1999), the Kuroshio off the Cape Shiono Misaki (Fig. 1a, Kimura and Sugimoto,
130 1993), the Kuroshio south of the Boso Peninsula (Fig. 1a, Itoh and Sugimoto 2008), the
131 Kuroshio Extension (Kouketsu et al., 2005; 2007), and the Gulf Stream in the upstream region
132 of the Cape Hatteras (Brooks and Bane, 1981; Lee and Atkinson, 1983). Such waves frequently
133 develop their amplitude, then developed tongue-like meander eventually detached from the
134 main stream of the current, entraining warm-lighter (cold-denser) water in the south (north) of
135 the front as anticyclonic (cyclonic) eddy (e.g., Yanagi et al., 1998). In addition to near surface,
136 at the mid-depths, such frontal disturbance could contribute to water-exchange. Kouketsu et al.
137 (2005) reported intrusion of low-salinity water into the subtropical gyre at the density of the
138 North Pacific Intermediate Water ($26.6\text{--}26.9 \sigma_\theta$; 300–600 dbar) associated with wave-like
139 structure with the horizontal length-scale of about 100 km along the Kuroshio Extension.
140 Therefore, if similar wave exhibits in the strait, such disturbance would be thought to play an
141 important role for water exchange across the front, and may contribute to faster acidification as
142 mentioned above (Wakita et al., 2021) through stirring and mixing of low pH water, in addition
143 to significant vertical mixing that pumps up materials such as nitrate (Tanaka et al., 2021)
144 including iron (Saitoh et al., 2008). However, observations that have resolution for such frontal

145 waves in the strait are rare although many repeated observations of ships and moorings were
146 conducted there, because of the intense velocity of the TWC and frequent ship traffic through
147 the strait.

148 HFR is one of the effective instruments for investigation of the frontal disturbances
149 including eddies (e.g., Schaeffer et al., 2017). Thus, employing the HFR that includes three
150 antennas installed at the eastern part of the strait (Fig. 1b), we investigated behavior of frontal
151 wave through examination of the axis variation of the TWC. In the present study, the time-series
152 of the surface velocity for three years provided by the HFR, that has horizontal resolution of
153 about 3 km and is temporal resolution of about 30 minutes, was employed. In this paper, as a
154 result, it will be revealed downstream propagation of the disturbance of the axis latitude with
155 increase of the amplitude to the downstream direction. Also, it will be shown that the
156 propagation speed is slower than that of advection due to surface current especially in the
157 seasons of the stratification. Internal stratification and velocity distribution obtained from
158 repeated shipboard observations along the fixed lines across the strait (Shiriya–Esan line, Fig.
159 1b) will be used for the investigation of the frontal waves in order to compare with the baroclinic
160 instability theory.

161 The remainder of the present study is as follows. Following section, we will provide
162 information of observation data and methods including surface velocity observed by the HFR,

163 shipboard observations, and propagation speed of the baroclinic instability waves based on the
164 theories provide by the previous studies. In the result section, first we will demonstrate the
165 seasonal variation of the TWC axis and shorter-term variations. Moreover, vertical distribution
166 of the stratification and velocity would be shown along the transection across the channel. Then,
167 propagation speed will be examined mainly based on the two-layer model concerning baroclinic
168 instability proposed by previous studies (e.g., Pedlosky, 1987; Itoh and Sugimoto, 2008). In the
169 final section, importance of the frontal wave in the strait will be discussed concerning short-
170 term variation of the gyre that develops from summer to autumn, and water mass modification.

171

172 **2 Methods**

173 **2.1 High Frequency Radar Velocity**

174 In order to monitor the surface current in the eastern part of the Tsugaru Strait, the
175 Mutsu Institute for Oceanography Ocean (MIO), Japan Agency for Marine-Earth Science and
176 Tecnology (JAMSTEC) has installed the monitoring system using the HFR (CODAR,
177 SeaSonde, 13.9 MHz) that has three antenna stations (Fig. 1c). Two of them are installed in the
178 Shimokita Peninsula, and the other is located at Hokkaido (Esan, Fig. 1c). The HFR provides
179 data whose horizontal resolution of the system is about 3 km, and the coverage of the
180 observation ranges from about 3 km to 60 km from each antenna. The surface current

181 distribution is calculated almost each 30 minutes by the system and uploaded at the site of MIO
182 Ocean Radar data Site for the eastern Tsugaru Strait (MORSETS;
183 <http://www.godac.jamstec.go.jp/morsets/e/top/>). Abe et al. (2020) reported that the root-mean-
184 square error between the HFR surface velocity and the sub-surface velocity obtained by
185 acoustic Doppler current profiler mounted on some ships (SADCP) in the Tsugaru Strait was
186 $30 (26) \square 10^{-2} \text{ m s}^{-1}$ in the east–west (north–south) direction. K21 suggested a similar accuracy
187 of the HFR velocity with that of Abe et al. (2020), while calling attention to an effect of the
188 surface wind on the HFR velocity especially during winter. The same HFR is used for the
189 surface current monitoring at the Tsushima Strait and at the Soya Strait (Fig. 1a), and some
190 previous studies have been demonstrated using them; the Tsushima Strait: Yoshikawa et al.
191 (2006; 2010), and the Soya Strait: Ebuchi et al. (2009). Yoshikawa et al. (2006) mentioned that
192 the root-mean-square velocity difference between the HFR and SADCP was $6.62\text{--}11.3 \square 10^{-2}$
193 m s^{-1} . Ebuchi et al. (2009) reported that the current estimated from the HFR agreed well with
194 those derived from SADCP with root-mean-square difference less than $25 \square 10^{-2} \text{ m s}^{-1}$. In the
195 present study, we employed data from 2017 to 2019 when the monitoring was stably conducted
196 by the all three antennas (the monitoring itself started since 2014).

197

198 **2.2 Analysis for the Temporal Variation of the Axis of the Tsugaru Warm Current**

199 First, we defined twenty-five sub-regions that is long in the north–south direction (Fig.
200 1c; R1–R25), and made spatial mean of zonal velocity in the east–west direction in the
201 subregion. Further, temporal mean of each 6-hour concerning the spatial mean was calculated
202 in each sub-region, to obtain the north–south distribution of the zonal velocity along each sub-
203 region. Then, the latitude where mean zonal velocity showed the maximum was defined as the
204 axis of the TWC. We investigated the seasonal mean location of the axis as well as its standard
205 deviation (Figs. 2 and 3). We also focused shorter-term variation of the axis (some examples
206 are shown in Fig. 4), and calculated spectrum of the temporal variation of the latitude of the
207 axis in each sub-grid, using data from 2018 to 2019 (Fig. 5; there was no missing of the HFR
208 data during the duration, but 2017). Moreover, we obtained low-pass-filtered data using a 5th
209 butterworth filter that has the cutoff timescale of 10-days (Fig. S1) in order to focus on
210 variations from 10 days to one month (Yasuda et al., 1988), for each three months. Then, we
211 made lag-correlation analysis of the time-series data with the low-pass concerning each sub-
212 region in relation to that in the reference sub-region near the eastern neck of the channel (R1;
213 140.96–140.04°E; Fig. 1c), expected as the region where disturbance of the axis would be
214 generated (Fig. 6). The timescale of the correlation peaks was regarded as the lag of arrival of
215 the disturbance, and using the distance between the reference sub-region and each sub-region,

216 propagation speed of the disturbance was estimated in each season (winter: January–March,
217 spring: April–June, summer: July–September, autumn: October–December) for each year (Fig.
218 7).

219

220 **2.3 Shipboard Observations**

221 Repeated observations were conducted along the SE-line between Shiriya and Esan
222 (Fig. 1b, Table 1) in almost each four seasons from 2009 to 2019 (Table 2) by three ships; the
223 training ship (T/S) Ushio-Marun and T/S Oshoro-Marun belonging to Hokkaido University, and
224 the research vessel (R/V) Wakataka-Marun belonging to the Japan Fisheries Research and
225 Education Agency.

226 Observations of temperature, salinity, and pressure were made as conductivity-
227 temperature-depth (CTD) observation in the cruises, using SBE 911 plus (Sea-Bird Scientific,
228 Inc.). Following the algorithms of UNESCO (United Nations Educational, Scientific and
229 Cultural Organization) (1983), depth was calculated from the value of the pressure and the
230 latitude of the stations. Then, each 1 m mean of temperature, salinity, and pressure was
231 estimated using linear interpolation. The potential density anomaly, σ_θ , was calculated using the
232 temperature, salinity, and pressure of each 1 m following Gill (1982). Then, an isodepth mean
233 of σ_θ in each season was calculated again (Fig. 8). After that, geostrophic velocity was

234 calculated following Pond and Pickard (1986) from each seasonal isodepth mean properties
235 between the adjacent stations (Fig. 9). The reference level was set to the bottom.

236

237 **2.3 Theoretical Estimation of Propagation Speed of the Baroclinic Instability in** 238 **the f -plain**

239 Since the meridional width of the eastern part of the Tsugaru Strait is narrow (~ 0.4
240 degree of latitude around the SE-line although north boundary is open, Fig. 1b) and thus impact
241 of latitudinal difference in the inertial frequency on the phenomena would be small. For this
242 reason, f -plain approximation would be adequate; the difference of the inertial frequency
243 between at the northern boundary of the strait $\sim 41.8^\circ\text{N}$ and the southern boundary $\sim 41.4^\circ\text{N}$ is
244 $< 1\%$. On the other hand, vertical structure is known to change drastically in each season (e.g.,
245 Sugimoto and Kawasaki, 1984). Therefore, it should be treated with caution for assumption of
246 the baroclinicity. In summer, intense pycnocline was reported (e.g., Matsuura et al., 2007;
247 Saitoh et al., 2008), which implies an applicability of the two-layer model (e.g., Pedlosky, 1987).
248 On the other hand, in winter, it is well known that surface mixed layer is developed and density
249 is vertically homogeneous (e.g., Sugimoto and Kawasaki, 1984). Thus, it is expected that
250 assumption of baroclinicity probably does not match well in winter, but we included winter in
251 the present investigation for comparison. In spring and autumn, stratification would be weaker

252 than that in summer. For this reason, we also employed the f -plain model that has an assumption
 253 of continuous stratification as well as constant vertical shear (Eady, 1949).

254 Using isodepth mean of the seasonal mean density anomaly from station SE3 to SE7,
 255 $\langle \sigma_\theta \rangle_{SE}$, we defined the depth of the boundary between the upper- and lower-layer as follows:

$$256 \quad \sigma_r = \sigma_2 - (\sigma_2 - \sigma_1)/e, \quad (1)$$

257 where σ_1 and σ_2 were potential density anomaly at 10 m and 250 m of $\langle \sigma_\theta \rangle_{SE}$, respectively. The
 258 depth has the potential density anomaly of σ_r was defined as H_1 , that is the upper-layer thickness
 259 (Fig. 10a). Then, following the derivation of Pedlosky (1987) (the equation 7.11.9), the phase
 260 speed of the baroclinic instability in the case of zero-planetary beta ($\beta=0$) in the two-layer
 261 stratified model as follows:

$$262 \quad c = \frac{U_1(K^2 + 2/R_2^2) + U_2(K^2 + 2/R_1^2)}{2(K^2 + 1/R_1^2 + 1/R_2^2)} \pm \frac{[-(U_1 - U_2)^2(4/R_1^2 R_2^2 - K^4)]^{1/2}}{2(K^2 + 1/R_1^2 + 1/R_2^2)} \quad (2)$$

263 where K , U_1 , and U_2 are the total wavenumber, the mean velocity of the upper-, and that of the
 264 lower-layers, respectively. And

$$265 \quad \frac{1}{R_n^2} = \frac{f_{41.5^\circ N}^2}{g' H_n}, \quad (3)$$

266 where H_n is the thickness of the n -th layer, and g' is the reduced gravity calculated as follows:

$$267 \quad g' = \frac{(\rho_2 - \rho_1)}{\rho_0} g, \quad (4)$$

268 where g is the gravitational acceleration (we employed it as 9.8 m s^{-2}), and ρ_1 , and ρ_2 , are mean
 269 density in the upper- and lower-layer, respectively. We defined the reference density, ρ_0 , as 1026

270 kg m^{-3} . We employed the inertial frequency at 41.5°N ($f_{41.5^\circ\text{N}} = \sim 18.1$ hour).

271 The instability occurs when $K^2 < 2/R_1R_2$. Assuming the wavenumber of the disturbance
272 observed in the strait would be small sufficiently for such instability, we employed the
273 propagation speed of the instability (real part of the Eq. 2), as mentioned in Itoh and Sugimoto
274 (2008), as follows:

275

$$276 \quad c = \frac{U_1(K^2 + 2/R_2^2) + U_2(K^2 + 2/R_1^2)}{2(K^2 + 1/R_1^2 + 1/R_2^2)}. \quad (5)$$

277

278 The upper-layer thickness, H_1 , was calculated as mentioned above, and the lower-layer
279 thickness was defined as the difference from 300 m minus H_1 , assuming that typical water depth
280 in the eastern part of the Tsugaru Strait beneath the axis is about 300 m (Fig. 1b). Then, U_1 (U_2)
281 was estimated using the spatial mean the geostrophic velocity in the upper-layer (lower-layer)
282 along the SE-line (generally stations SE3–SE7, but SE4–6 in winter; Fig. 10b) in each season.
283 When the horizontal wave number K is sufficiently smaller than $1/R_n$, in other words, the
284 wavelength of the frontal wave is far longer than the deformation radii, the Eq. 5 can be further
285 simplified as follows:

$$286 \quad c = \frac{U_1(1/R_2^2) + U_2(1/R_1^2)}{(1/R_1^2 + 1/R_2^2)}. \quad (6)$$

287 This equation indicates that the propagation speed, c , takes a value between U_1 and U_2 with

288 $1/R_n^2$, as the weighting function.

289 In addition to the two-layer model, for comparison, we calculated the phase speed of
290 the baroclinic instability in the continuous stratification and constant vertical shear of zonal
291 velocity following Eady's theory as follows:

$$292 \quad c_E = \frac{U_s}{2} \pm \frac{U_s}{\mu} \sqrt{\left(\frac{\mu}{2} - \coth \frac{\mu}{2}\right) \left(\frac{\mu}{2} - \tanh \frac{\mu}{2}\right)}, \quad (7)$$

293 where U_s is the surface velocity, and $\square = L_D K$. L_D is deformation radius defined by $L_D = NH/f_0$
294 (N is Brunt-Väisälä frequency in the continuous stratification as mentioned later; H and f_0 are
295 layer thickness and inertial frequency at the reference latitude, respectively). Note that
296 considering occurrence of the instability, we defined the propagation speed in the Eady's case
297 as a real part of the Eq. 7, that is $c_E = U_s/2$. Here, U_s was calculated as a mean geostrophic
298 velocity for upper 10 m.

299 It should be also noted that in order to determine the wavelength of the disturbance in
300 each season, we employed the maximum growth rate of Eady's case, $\square = 1.61$. We calculated
301 N as follows:

$$302 \quad N = \frac{1}{H} \int \sqrt{-\frac{g}{\rho_0} \frac{\partial \langle \sigma_\theta \rangle_{SE}}{\partial z}} dz. \quad (8)$$

303 For estimation of L_D , H and f were set as 300 m and $f_{41.5^\circ N}$, respectively. Using these equations
304 and parameters, we calculated the propagation speed of the baroclinic instability in some cases,
305 and compared them to the propagation speed of the observed disturbance of the TWC's axis in

306 each season (Fig. 7).

307

308 **3 Results**

309 **3.1 Frontal waves detected from the surface current distribution observed by**

310 **HFR**

311 First, seasonal distribution of the axis was shown briefly, before demonstration of the
312 short-term variations of the axis. Fig. 2 showed seasonal mean location of the axis in each sub-
313 region together with standard deviation. From the eastern neck of the channel ($\sim 141.0^\circ\text{E}$) to the
314 Shiriya Spur ($\sim 141.5^\circ\text{E}$), whereas the axis located relatively south (south of 41.6°N) during
315 winter and spring (Fig. 2a and b, respectively), it moves northward from summer to autumn
316 (north of 41.6°N , Fig. 2c and d, respectively). This seasonal movement has been already
317 reported by the previous studies (e.g., Rosa et al., 2007; Abe et al., 2020; Y21; K21). The
318 velocity of the axis was generally faster (slower) in summer (winter) reaching 1.0 (0.6) m s^{-1}
319 west of the Shiriya Spur. With respect to the east of the spur, the velocity was slow in winter
320 and spring (Fig. 2a and b, respectively). In contrast, relatively larger velocity and somewhat
321 straightforward flow pattern in the east–west direction was observed in summer (Fig. 2c).
322 Standard deviation of the axis latitude generally increased to the downstream especially in the
323 region of 141.0 – 141.6°E , that is west to the Shiriya Spur (Fig. 3). As an exception, in the season

324 of winter the standard deviation showed a small peak at $\sim 141.4^\circ\text{E}$, at the west-side of the Shira
325 Spur (Fig. 3a). In spring, the standard deviation increased monotonically with increase of the
326 longitude in the region west of 141.8°E (Fig. 3b), while in summer, the standard deviation
327 increased steeply in the range of $141.4\text{--}141.6^\circ\text{E}$ (Fig. 3c). Concerning autumn, the distribution
328 of the standard deviation in October (December) was similar with that in spring (winter) (Fig.
329 3d).

330 Besides the seasonal movement of the axis as mentioned above, shorter-term
331 oscillation within several dozen days was observed. We showed some examples of such
332 variation as Fig. 4. In summer of 2017, large amplitude oscillation of the axis in the north–south
333 direction was recognized especially north the Shiriya Spur as ridge-shaped distribution that has
334 one north convex peak with the east–west scale of ~ 50 km (Fig. 4a). On the other hand, in
335 winter of 2018, short-term variations were also active (Fig. 4b), but multiple peaks of the
336 meander were demonstrated, and the horizontal scale in the east–west direction of the wave-
337 like meandering (peak-to-peak) was inferred as ~ 40 km. The short-term variations were also
338 observed in the other seasons (not shown).

339 We estimated power spectral density concerning the oscillation of the axis in each sub-
340 region using data from 2018 (January 1st) to 2019 (December 31st) when the surface velocity
341 continuously observed (Fig. 5). The spectrum indicated remarkable peaks around timescale of

342 13.66 days as well as that of double of it (27.32 days) in the western regions from the eastern
343 neck of the channel (R1) to the Shiriya Spur (around R12; Fig. 1b and c). Peaks of the timescale
344 of ~ 13.7 days and ~ 27.3 days became obscured in the regions east to the spur. The variation
345 with ~ 13.7 days was consistent with that reported near the eastern neck of the channel (around
346 Esan, Fig. 1b) by Tanno et al. (2005).

347 In order to examine the relationship of the periodical disturbance among each sub-
348 region, we defined the sub-region R1 (Fig. 1c) as the reference where the disturbance was
349 expected to be generated, and then, we calculated lag correlation of the time-series of the axis
350 latitude between the reference sub-region and other sub-regions (R2–R25) (Fig. 6). In order to
351 focus the variation that has longer timescale than 10 days (Yasuda, 1988), we calculated the
352 low-pass-filtered data using the fifth power butterworth filter that has the cutoff timescale of
353 10-days (Fig. S1). Significant positive peak was recognized in R2–16, showing increase of the
354 lag with the increase of the distance from the reference sub-region (Fig. 6). The lag peaks
355 showed a cyclical characteristic in each sub-region with a cycle of ~ 14 days (Fig. 6).

356 We plotted the lag-time of the correlation peaks (shown by triangles in Fig. 6)
357 concerning the positive range (y -axis), against the distance from the reference sub-region (x -
358 axis) (Fig. 7). Here, in addition to the first cycle, the lag of the second cycle starting at 13.7
359 days, is also shown as the gray plot. The lag-correlation was calculated in four seasons (3

360 months) of each year (2017–2019). We also estimated the timescale of advection estimated
361 from the mean surface velocity U_1 from R1 to R25 (gray broken lines with smaller slope in Fig.
362 7). Linear increasing of lag-time of the observed disturbance with increase of the distance
363 (symbol plots in Fig. 7) was clearly demonstrated in spring and summer. The slopes of the
364 disturbance (symbol plots in Fig. 7) indicated seasonal variation, showing the largest angle in
365 spring. We regarded the slope as the propagating speed of the propagation of the axis
366 meandering. That is, it was suggested that the propagation speed of the observed disturbance
367 became slowest in spring. In winter, propagation of the disturbance of the TWC's axis was
368 unclear in 2017 and 2018 (Fig. 7d). To sum up, the results showed that the longer timescale
369 concerning the propagation of the disturbance was frequently recognized than that estimated
370 from the surface advection, especially in the seasons from spring to autumn in the regions west
371 of the SE-line (Fig. 7a–c).

372 The slower propagation speed than that of advection suggested the disturbance of the
373 axis would not be simply advected by the surface current. Thus, we suspected the propagation
374 of the disturbance of the TWC's axis as propagation of the frontal waves as reported in other
375 regions (e.g., Brooks and Bane, 1981; Lee and Atkinson, 1983; Sugimoto et al., 1988; Kimura
376 and Sugimoto, 1993; Kouketsu et al., 2005; Itoh and Sugimoto, 2008), as mentioned in the
377 Introduction. Since meridional range of the frontal disturbance in the strait is relatively smaller

378 (Figs. 3 and 4) than those reported by the previous studies in the western boundaries, thus, it is
379 easy to think that the f -plain assumption seems to be reasonable. Whereas, structure of
380 stratification in the strait was known to be drastically changed in each season as mentioned
381 above (e.g., Nishida et al. 2003; Saitoh et al., 2008). Thus, to examine the application of the
382 two-layer baroclinic instability theory, we would demonstrate the seasonal vertical structure
383 across the strait concerning the density and velocity in the next subsection.

384

385 **3.2 Internal structure concerning the stratification and velocity across the** 386 **channel obtained from shipboard observations**

387 The HFR revealed near surface disturbance that had slower propagation speed than
388 that caused by advection of the surface current especially in stratified season as mentioned in
389 the previous subsection. Such downstream-propagating disturbance with increasing amplitude
390 might be expected as baroclinic instability along front. To test the theory of the instability under
391 the two-layer model condition as described in the Material and Methods section, internal
392 structure including the upper- and lower-layer thickness and velocity there, are required (Eq. 5).
393 Thus, in this subsection, we would show seasonal distribution of the thickness and velocity
394 across the eastern part of the strait (SE-line; Fig. 1b) obtained from shipboard observations of
395 2009–2019 (Table 2).

396 Seasonal mean of the salinity showed that higher salinity water located the southern
397 side of the strait (Fig. 8), indicating a remarkable front around the center of the strait ($\sim 41.7^\circ\text{N}$
398 except for winter; $\sim 41.6^\circ\text{N}$ in winter). The location of the front corresponded well to that of the
399 axis of the TWC (Fig. 2). Moreover, this salinity distribution suggested that high-temperature
400 and high-salinity water of the TWC was distributed along the southern coast, while lower-
401 temperature and lower-salinity water affected by the coastal Oyashio was located in the northern
402 side of the strait as reported by the previous studies (Kono et al., 2004; Rosa et al., 2007; Saitoh
403 et al., 2008; Kuroda et al. 2012; Wakita et al., 2021). The level of the salinity at the core of the
404 water of the TWC was highest in summer (Fig. 8b). In autumn, salinity contrast in the north–
405 south direction weakened showing a general increase of the salinity (>34.8 psu) in the strait
406 (Fig. 8c).

407 Also, seasonal mean transection along the SE-line of the potential density anomaly, σ_θ ,
408 indicated remarkable variation, showing strong (weak) stratification in summer (winter) (Fig.
409 8). In winter, mean σ_θ in the channel were estimated as ~ 26.5 σ_θ and vertically almost
410 homogeneous. In contrast, steep surface pycnocline at the subsurface, ~ 50 m, was estimated as
411 a mean distribution in summer, showing that the surface (near bottom) potential density
412 anomaly was ~ 23.0 (~ 26.0) σ_θ . In spring and autumn, although vertical difference of the density
413 was weaker than that in summer, stratification was also developed.

414 Similar as the potential density anomaly distribution, geostrophic velocity distribution
415 along the same transection also showed remarkable seasonal variation (Fig. 9). In winter, the
416 velocity distribution was expected to be vertically homogeneous and the magnitude of the
417 eastward flow was weak. In the other seasons when stratification was developed, remarkable
418 eastward current core ($>1 \text{ m s}^{-1}$) was calculated near surface. In summer and autumn, opposite
419 westward flow was estimated south of the intense eastward current in the upper-layer. It should
420 be noted here that the estimation of eastward geostrophic velocity in autumn might be
421 overestimate due to the westward bottom current near the bottom around stations 3–4 that was
422 suggested by the SADCP observation (not shown).

423 Seasonal distribution of σ_θ and velocity suggested the obvious stratified situation in the
424 strait except for winter. This result was consistent with that reported by many previous studies
425 (e.g., Sugimoto and Kawasaki, 1984; Nishida et al., 2003; Matsuura et al., 2007; Saitoh et al.,
426 2008). Thus, we estimated the representative values of the upper- and lower-layer thickness,
427 and velocity in each season using the Eq. 1. The depths of the upper-layer, H_1 , in each season
428 were estimated as 63 m (spring), 69 m (summer), 124 m (autumn), and 152 m (winter) (denoted
429 by the triangles in Fig. 10a). The depths, H_1 , were indicated as magenta horizontal broken lines
430 in Figs. 8 and 9, and the estimation seemed reasonable as the boundary of the upper- and lower-
431 layer over the transection. Note that the remarkable two-layer like distribution was

432 demonstrated in summer, but in the other stratified season (spring and autumn), the vertical
433 change in the density seemed somewhat gentle (Fig. 10a). This characteristic was similar
434 regarding seasonal change in the vertical structure of geostrophic velocity (Fig. 10b). Thus, not
435 only the approximation of the two-layer model, but also that of the continuous stratification was
436 also investigated in the present study as mentioned in the next subsection (3.3), using the Eq. 7.

437

438 **3.3 Investigation of the propagation speed of the frontal disturbance**

439 Using the parameters estimated in the previous subsection, and the Eqs. 5 and 7, we
440 calculated the propagation speed of the baroclinic instability in order to compare them to the
441 propagation speed of the disturbance observed by the HFR (Fig. 7). We employed the
442 wavelength of baroclinic instability of each season as 70 km (spring), 145 km (summer), 98 km
443 (autumn), and 43 km (winter), respectively, assuming the maximum growth case in the Eady's
444 model. This wavelength satisfies the instability condition of the two-layer model (e.g., the
445 equation 7.11.10 of Pedlosky, 1987).

446 In spring, the propagation speed of the observed disturbance was similar with that of
447 the two-layer model (0.14 m s^{-1} ; Fig. 7a) in the distance range of 30–80 km, although outliers
448 were shown in the downstream of the Shiriya Spur in 2018. In contrast, the propagation speed
449 of the Eady's model were somewhat slower than that of the observed disturbance. In summer,

450 the propagation speed of the baroclinic instability $\sim 0.20 \text{ m s}^{-1}$ was also consistent with that of
451 the observed disturbance especially in 2019 (Fig. 7b). It should be noted that, the zonal velocity
452 beneath the axis of the TWC was smaller in 2018 than that in 2019 according to the SADC
453 observation, showing a consistency with slower propagation speed in 2018 (not shown).
454 Concerning autumn, because the propagation of the disturbance of the axis was not clear in 40–
455 80 km, thus it is difficult to detect clear correspondence between them (Fig. 7c). However, when
456 a continuous propagation of the disturbance was assumed between that in 0–40 km and 80–110
457 km in 2017 (upward triangles in Fig. 7c), the propagation speed seemed to show a similarity
458 with that of the two-layer model (0.28 m s^{-1}) and Eady's model. In the season of winter, the
459 propagation of the disturbance was not clear in 2017 and 2018 (Fig. 7d). In 2019, the
460 distribution of the downward triangles is not uniform in slope on the 0–100 km scale. Moreover,
461 the propagation speed of the two-layer model was far smaller than that of the observed
462 disturbance because of weak eastward geostrophic velocity. In winter, stratification was very
463 weak in the region (Fig. 10a). Thus, caution should be required in the interpretation of the
464 propagation of the disturbance in this season as a baroclinic instability.

465 As a summary of this subsection, it could be said that the propagation speed in stratified
466 season showed a well agreement with that of the baroclinic instability in the case of the two-
467 layer model, especially in spring and summer. Therefore, the propagation of the axis disturbance

468 of the TWC observed by the HFR in the seasons was suggested as that closely related with the
469 baroclinic instability.

470

471 **4 Discussion**

472 **4.1 Compatibility of the two-layer model to the observed disturbance, and** 473 **comparison with frontal waves in other regions**

474 In the present study, we examined the consistency of the propagation speed of the
475 disturbance of the TWC's axis observed by the HFR with the propagation speed based on the
476 theory of the two-layer baroclinic instability in the f -plane (Fig. 7). Then, close value of the
477 propagation speed of the disturbance of the TWC's axis observed by the HFR with that
478 calculated assuming the two-layer model was indicated in the stratified season, such as spring
479 and summer in a cycle of ~ 13.7 days (Fig. 7a, and b). In addition to the two-layer model, we
480 also examined the propagation speed based on the Eady's theory. Although the magnitude of
481 the propagation speed based on the Eady's theory was similar with that of the observed
482 disturbance in summer and autumn, however, they were dissociated in the downstream region
483 (>40 km, Fig. 7a) in spring. Also, it should be noted that, considering the characteristic of the
484 internal structure, the two-layer assumption also seemed better than that of continuous
485 stratification especially in summer. The two-layer assumption may be better for the autumn

486 season as well. The geostrophic velocity in the lower layer in autumn may perhaps be
487 overestimated, because some of the observed disturbances seemed slower than that of the
488 Eady's theory. In the SADPC observation, westward velocity was sometimes observed near the
489 bottom between the stations 3–4 (not shown), which may be due to topographic wave
490 propagation from the north related to the wedge-shaped topography in the eastern part of the
491 strait (Figure 1b). Moreover, we would like to note that more careful investigations are needed
492 for determination of the dominating wavelength in the region, since the dominant wavelength
493 was assumed based on the Eady's theory.

494 The observed propagation speed in summer (0.20 m s^{-1}) was similar with that
495 estimated by Itoh and Sugimoto (2008) near the Boso Peninsula (Fig. 1a; $0.22\text{--}0.30 \text{ m s}^{-1}$ with
496 the wavelength of 220–380 km), and Kouketsu et al. (2007) in the Kuroshio Extension (0.20--
497 0.30 m s^{-1} with the wavelength of ~ 200 km). In contrast, the propagation speed was smaller
498 than that reported in the Gulf Stream by Lee and Atkinson (1983) ($0.50\text{--}0.70 \text{ m s}^{-1}$ with the
499 wavelength of 300–500 km). Although the water depth was different between the TWC and the
500 open ocean currents such as the Kuroshio and the Kuroshio Extension, the effect of ratio
501 concerning the thickness of the upper- to the lower-layer would possibly be accountable for this
502 similarity. The slower propagation speed in springtime (0.14 m s^{-1}) may be due to the strength
503 of the surface currents ($U_1 = 0.20 \text{ m s}^{-1}$) that was weaker than that in the summer season ($U_1 =$

504 0.36 m s⁻¹).

505 As other issues to be considered, we would like to mention the topography. An impact
506 of the characteristic topography on the instability was not considered in the present study. The
507 steep increase in amplitude over the Shiriya Spur in summer (Fig. 3c), and the bypassing
508 movement of the axis around the spur (Fig. 4a) may suggest the influence of the topography.
509 On the other hand, short-term variation of the axis also indicated a riding up of the TWC over
510 the spur sometimes (Fig. 4a). The outliers in Fig. 7a around the spur in 2018 (with lag of ~10
511 days) may be also related with the topographic effect. Y21 suggested that the TWC tends to
512 flow over the spur with increase of inertia in winter. Thus, the relationship between the
513 topographic effect and the path of the TWC should be also investigated as an issue to address
514 in relation to intensification of the inertia of the TWC.

515

516 **4.2 Frontal Disturbance in the Weak Stratified Season**

517 Figure 4 implies that the length-scale of the frontal disturbance in the east–west
518 direction seemed smaller in winter than that in summer. In winter, as estimated L_D was small, it
519 might occur the scale of the instability become smaller. However, as mentioned above, the
520 accuracy of the application of the baroclinic instability is suspicious for the homogenous density
521 distribution (Fig. 10a). Instead, barotropic disturbance along the shelf might be plausible. In

522 relation with the barotropic phenomena, using idealized topography, Ohshima (1994) pointed
523 out scattering of the Kelvin wave to the higher mode shelf waves at the eastern outlet of the
524 strait (northeast corner of the Shimokita Peninsula) based on a numerical model. Although there
525 is difference in the topography between the idealized one of Ohshima (1994) and reality, similar
526 scattering might be caused by the topography in the eastern neck of the channel ($\sim 141.1^\circ\text{N}$),
527 because the mouth of the strait becomes wider there in the eastward direction (Fig. 1b). These
528 shelf waves might affect the short-term disturbance of the TWC's axis along the north coast of
529 the Shimokita Peninsula in winter (Fig. 4). Especially higher mode of the shelf waves might
530 cause slow propagation of the disturbance of the axis (Fig. 7d, that in the range of 0–40 km of
531 2019). Moreover, the eastward propagation of the disturbance, which was more pronounced in
532 winter (Fig. 7d, 2018), may imply the influence of topographic trapping waves from north to
533 east associated with the wedge-shaped topography in the eastern part of the strait as mentioned
534 above (Fig. 1b). Wintertime behavior of the TWC should be examined using the HFR and
535 numerical model in future.

536

537 **4.3 Impact of the Disturbance on the Short-term Variation of the Tsugaru Gyre**

538 As mentioned in the Introduction, observational studies by Yasuda et al. (1988) have
539 reported short-term fluctuations of the large anticyclonic gyre which timescale was 20–30 days

540 (the direction of the major axis of the gyre's elliptical distortion rotated clockwise with these
541 fluctuations). Kubokawa (1991) showed in his numerical experiment that such clockwise
542 variations along the gyre can be successfully reproduced by varying the volume transport of the
543 TWC that has relatively lower potential vorticity by changing the latitude of the front of the
544 TWC at the outlet of the strait in the north–south direction. Therefore, it is quite possible that
545 the north–south frontal disturbances observed in this study could influence such short-term
546 variations of the large anticyclonic gyre. At the eastern outlet of the strait (e.g., R12; 141.42–
547 141.50°E), a peak of ~27.3 days was also demonstrated in the spectrum of the frontal
548 disturbance (Fig. 5), which is consistent with the periodicity reported by Yasuda et al. (1988).
549 On the other hand, although the period of ~13.7 days was also recognized at the outlet of the
550 strait, the period is a little shorter than the timescale reported by Yasuda et al. (1988). Thus, it
551 is necessary to examine whether the shorter-term variability of the gyre at this timescale also
552 occurs, as a future work. Since the period of the frontal disturbance is in good agreement with
553 the ~13.7 days cycle (and its double length) that prevails in the Tsugaru Strait and the Soya
554 Strait (Onishi et al., 2004; Tanno et al. 2005; Ebuchi et al., 2009), the result suggested that tides
555 may play an important role on the frontal disturbance. However, it is not unclear yet that what
556 specific processes are involved between them. This is another issue that needs to be continued
557 to be examined. The short-term variability of the large anticyclonic gyre (gyre mode) is

558 considered to be closely related to changes in the fishing grounds of pelagic fishes around the
559 Shimokita Peninsula (e.g., Sato 1974, Hirai et al. 1988), and thus, the elucidation and
560 forecasting of the excitation process is an important issue in terms of contributing to the
561 prediction of fishing grounds. If the relationship between the tide and the short-term variability
562 of the gyre is clarified, there is a high possibility that it will eventually contribute to the
563 prediction of the fishing grounds.

564

565 **4.3 Importance of the Baroclinic Instability on the Water modification in the** 566 **Tsugaru Strait**

567 As pointed out by the many previous studies, the development of the frontal wave
568 could affect water mass exchange in the direction across the front (e.g., Yanagi et al., 1998;
569 Kouketsu et al. 2005). In the region of the frontal disturbance was observed by the HFR, the
570 low temperature and salinity water called as the coastal Oyashio Water sometimes juts from
571 north (e.g., Kuroda et al. 2012; Wakita et al., 2021). Thus, the development of the disturbance
572 may contribute to the transport of such cold (warm) water to the northern coast of the Shimokita
573 Peninsula (coastal area of Hokkaido). Actually, the north–south contrast of salinity in the strait
574 rapidly weakened in autumn (Fig. 8c), the after season of summer when the remarkable
575 occurrence of the instability would be expected. Also, although it is a case in winter, coastal

576 monitoring conducted by the MIO revealed that intense negative anomaly from the annual mean
577 (about 4 °C lower) in 2014 around the northern coast of the Shiomokita Peninsula. In this year,
578 landing of the yellow goosfish (*Lophius litulon*) was poor, which brought large social impact
579 around the fisheries communities along the northern coast of the peninsula. Thus, investigation
580 of the mechanisms of such water exchange and subsequent forecast are important not only for
581 science but also for the society.

582 In addition, the instability may also affect vertical mixing of the waters through some
583 mechanisms such as local intensification of the vertical shear. Kouketsu et al. (2007) suggested
584 that intrusion of the denser water at the mid-depths could occur in the region of the crest to the
585 trough of the upper frontal wave in the Kuroshio Extension due to the baroclinic instability.
586 Thus, local enhancement of the turbulence associated with such intrusions could be also
587 expected, which might contribute to the characteristic distribution of the turbulence intensity
588 along stream direction. The grasp of the along stream structure of the turbulence and fluxes
589 would bring more accurate estimation of them in the frontal region as a progress study of the
590 previous understanding such as Kaneko et al. (2012; 2013). The observations of the turbulence
591 and fluxes including low pH water will be conducted in near future. Moreover, these studies of
592 water mass exchanges and vertical mixing (including the present study) would also contribute
593 to improve understanding of the mechanism of the faster acidification the Tsugaru Strait than

594 that in the open ocean (Wakita et al., 2021).

595

596

597 **5 Conclusions**

598 This study focused on the front, that is the current axis, in the eastern part of the
599 Tsugaru Strait where the low-temperature, low-salinity water of the Oyashio system and the
600 high-temperature, high-salinity water of the Tsugaru Warm Current meets, using data provided
601 by the HFR that enables quasi-real time monitoring of a wide area, and the CTD ship data
602 accumulated over 10 years. The north–south disturbance of the axis propagated eastward
603 (downstream) with increasing amplitude, especially during the stratification period, with a
604 periodicity of about 14 days, which is the predominant period of tide in this region. This result
605 suggested a possibility of baroclinic instability near the front in this region. These disturbances
606 would affect the north–south water mass mixing in the strait and the short-term variability of
607 the Tsugaru warm water gyre that develops on the Pacific side during the stratification period.
608 In conclusion, this study suggests that tidal fluctuations in the Tsugaru Strait could cause short-
609 term changes in the gyre of the TWC outflow through the propagation along the water mass
610 front, contributing to the understanding of the individual findings as an integrated phenomenon.

611

612 **Abbreviations**

613 CTD: conductivity-temperature-depth (observation); HFR: High Frequency Radar; JAMSTEC:
614 Japan Agency for Marine-Earth Science and Technology; K21: Kaneko et al., submitted to GRL
615 as “The role of an intense jet in the Tsugaru Strait in the formation of the outflow gyre revealed
616 using high-frequency radar data”; MIO: Mutsu Institute for Oceanography Ocean; MORSETS:
617 MIO Ocean Radar data Site for the eastern Tsugaru Strait; R/V: research vessel; SADCP:
618 acoustic Doppler current profiler mounted on some ships; SE: Shiriya–Esan (line);
619 T/S: training ship; TWC: Tsugaru Warm Current; UNESCO (United Nations Educational,
620 Scientific and Cultural Organization); Warm Current revealed by high-frequency ocean radar”;
621 Y21: Yasui et al., submitted to Journal of Oceanography as “Seasonal pathways of Tsugaru

622

623 **Declarations**

624 **Availability of data and material**

625 The datasets of surface velocity obtained from the HFR analyzed for this study can be
626 distributed through the Mutsu Institute for Oceanography, JAMSTEC
627 (<https://www.godac.jamstec.go.jp/morsets/e/top/>). The other data analyzed for this study are
628 available from the corresponding author upon reasonable request.

629

630 **Competing interests**

631 The authors declare that they have no competing interest.

632

633 **Funding**

634 The authors did not receive support from any organization for the submitted work.

635

636 **Authors' contributions**

637 HK conceptualized the present study, and performed analysis of the data obtained from the HFR

638 and shipboard observations, visualization of figures, and writing the manuscript reflecting the

639 comments from all authors. HK, TT, HA, MW, KS, DH, and TO devised the observation plan

640 and engaged the in-situ data collection together with ST. SW and KS projected an introducing

641 and installing the HFR, and they also administrated and supervised concerning the continuous

642 observation of the HFR. YS was responsible for the management and retention of the HFR data.

643 All authors were contributed to discussions of the results and comments on the manuscript.

644

645 **Acknowledgements**

646 The authors acknowledge the help of the staff of the Mutsu Institute for Oceanography and the

647 Research Institute for Global Change of JAMSTEC. We also sincerely acknowledge the

648 captains and crews of T/S *Ushio-Maru*, *Oshoro-Maru*, and R/V *Wakataka-Maru* for their warm
649 cooperation during sample collection and hydrographic measurement for cruises of 2009–2019.
650 We appreciate the technical support staff from Marine Work Japan. We also thank T. Yasui,
651 T. Hashimukai, T. Nakayama, and S. In for their helpful comments. We refereed following
652 preprint studies in the present study; 1) H. Kaneko, K. Sasaki, H. Abe, T. Tanaka, S. Watanabe,
653 T. Okunihisi, Y. Sato, and S. Tatamisashi, “The role of an intense jet in the Tsugaru Strait in the
654 formation of the outflow gyre revealed using high-frequency radar data” submitted to GRL, and
655 2) T. Yasui, H. Abe, T. Hirawake, K. Sasaki, and M. Wakita, “Seasonal pathways of Tsugaru
656 Warm Current revealed by high-frequency ocean radar”, submitted to Journal of Oceanography.

657

658 **References**

659 Abe H, Sasaki K, Yasui T, Wakita M (2020) Observation of Tsugaru warm current by High
660 Frequency Radar and preliminary result for its prediction. *Kaiyo Monthly*. 52:312–316. (in
661 Japanese)

662 Astor YM, Lorenzoni L, Thunell R, Varela R, Muller-Karger F, Troccoli L, Taylor GT, Scranton
663 MI, Tappa E, Rueda D (2013) Interannual variability in sea surface temperature and fCO₂
664 changes in the Cariaco Basin. *Deep Sea Res Part II*, 93:33–43.
665 <http://dx.doi.org/10.1016/j.dsr2.2013.01.002>.

666 Brooks DA, and Bane JM (1981) Gulf-stream fluctuations and meanders over the Onslow Bay
667 upper continental-slope. *J Phys Oceanogr* 11:247–256. [https://doi.org/10.1175/1520-0485\(1981\)011<0247:GSFAMO>2.0.CO;2](https://doi.org/10.1175/1520-0485(1981)011<0247:GSFAMO>2.0.CO;2).

668

669 Conlon DM (1982) On the outflow modes of the Tsugaru Warm Current. *La mer* 20:60–64.

670 Dore JE, Lukas R, Sadler DW, Church MJ, Karl DM (2009) Physical and biogeochemical
671 modulation of ocean acidification in the central North Pacific. *Proc Natl Acad Sci USA* 106:
672 12,235–12,240. <http://dx.doi.org/10.1073/pnas.0906044106>.

673 Ebuchi N, Fukamachi Y, Ohshima KI, Wakatsuchi M (2009) Subinertial and seasonal variations
674 in the Soya Warm Current revealed by HF ocean radars, coastal tide gauges, and bottom-
675 mounted ADCP. *J Oceanogr* 65:31–43. <https://doi.org/10.1007/s10872-009-0003-2>.

676 Eady ET (1949) Long waves and cyclone waves. *Tellus* 1:33–52.
677 <https://doi.org/10.1111/j.2153-3490.1949.tb01265.x>.

678 Gill AE (1982) *Atmosphere-Ocean Dynamics*. Academic Press, San Diego

679 Hirai M, Ogawa Y, Okuda K, Yasuda I, Yamaguchi H (1988) Fluctuation of Hydrographic
680 Conditions in Relation to the Formation, Movement and Disappearance of Purse Seine Fishing
681 Grounds of Chub Mackerel in Waters off Sanriku, Northeastern Japan. *Bull Tohoku Reg Fish*
682 *Res Lab* 50:133–151 (in Japanese with English abstract)

683 Isobe A (1999) On the origin of the Tsushima Warm Current and its seasonality. *Cont. Shelf*

684 Res. 19:117–133. [https://doi.org/10.1016/S0278-4343\(98\)00065-X](https://doi.org/10.1016/S0278-4343(98)00065-X).

685 Ito T, Togawa O, Onishi M, Isoda Y, Nakayama T, Shimizu S, Kuroda H, Iwahashi M, Sato C
686 (2003) Variation of velocity and volume transport of the Tsugaru Warm Current in the winter
687 of 1999–2000. *Geophys Res Lett* 30:11(1–4). <https://doi.org/10.1029/2003GL017522>.

688 Itoh S, Sugimoto T (2008) Current variability of the Kuroshio near the separation point from
689 the western boundary. *J Geophys Res* 113:C11020. <https://doi.org/10.1029/2007JC004682>.

690 James C, Wimbush M, Ichikawa H (1999) Kuroshio meanders in the East China Sea. *J Phys*
691 *Oceanogr* 29: 259–272. [https://doi.org/10.1175/1520-0485\(1999\)029<0259:KMITEC>2.0.CO;2](https://doi.org/10.1175/1520-0485(1999)029<0259:KMITEC>2.0.CO;2).

692

693 Kaneko H, Yasuda I, Itoh S (2012) Observations of the structure of turbulent mixing across the
694 Kuroshio. *Geophys Res Lett* 39:L15602, <https://doi.org/10.1029/2012GL052419>.

695 Kaneko H, Yasuda I, Itoh S (2013) Observations of vertical turbulent nitrate flux across the
696 Kuroshio. *Geophys Res Lett* 40:3123–3127, <https://doi.org/10.1002/grl.50613>.

697 Kaneko H, Yasuda I, Itoh S, Ito S (2021) Vertical turbulent nitrate flux from direct
698 measurements in the western subarctic and subtropical gyres of the North Pacific. *J Oceanogr*
699 <https://doi.org/10.1007/s10872-020-00576-0>.

700 Kawasaki Y, Sugimoto T (1984) Experimental Studies on the Formation and Degeneration
701 Processes of the Tsugaru Warm Gyre. Elsevier Oceanography Series, vol 39, Elsevier, pp 225–

702 238, [https://doi.org/10.1016/S0422-9894\(08\)70302-7](https://doi.org/10.1016/S0422-9894(08)70302-7).

703 Kida S, Qi B, Yang J, Lin X (2016) The annual cycle of the Japan Sea Throughflow. *J Phys.*

704 *Oceanogr.* 46:23–39. <https://doi.org/10.1175/JPO-D-15-0075.1>.

705 Kida S, Takayama K, Sasaki YN, Matsuura H, Hirose N (2020) Increasing trend in Japan Sea

706 Throughflow transport. *J Oceanogr.* <https://doi.org/10.1007/s10872-020-00563-5>.

707 Kimura S, Sugimoto T (1993) Short-period fluctuations in meander of the Kuroshio path off

708 Cape Shiono-misaki. *J Geophys Res* 98(C2):2407 – 2418. <https://doi.org/10.1029/92JC02582>.

709 Kono T, Foreman M, Chandler P, Kashiwai M (2004) Coastal Oyashio south of Hokkaido,

710 Japan. *J Phys Oceanogr* 34: 1477–1494. [https://doi.org/10.1175/1520-](https://doi.org/10.1175/1520-0485(2004)034<1477:COSOHJ>2.0.CO;2)

711 [0485\(2004\)034<1477:COSOHJ>2.0.CO;2](https://doi.org/10.1175/1520-0485(2004)034<1477:COSOHJ>2.0.CO;2).

712 Kouketsu S, Yasuda I, Hiroe Y (2005) Observation of frontal waves and associated salinity

713 minimum formation along the Kuroshio Extension. *J Geophys Res* 110:C08011,

714 <https://doi.org/10.1029/2004JC002862>.

715 Kouketsu S, Yasuda I, Hiroe Y (2007) Three-dimensional structure of frontal waves and

716 associated salinity minimum formation along the Kuroshio Extension. *J Phys Oceanogr*

717 37:644–656. <https://doi.org/10.1175/JPO3026.1>.

718 Kubokawa A. (1991) On the behavior of outflows with low potential vorticity from a sea strait.

719 *Tellus A* 43:168–176. <https://doi.org/10.1034/j.1600-0870.1991.t01-1-00007.x>.

720 Kuroda H, Isoda Y, Takeoka H, Kuma K, Honda S, Matsuura H, Saitoh Y, Takata H, Iwade S,
721 Wagawa T, Kobayashi N (2012) Intrusion of the Oyashio water into the eastern mouth of
722 Tsugaru Strait in early summer, 2003. *Cont. Shelf Res* 32: 36–46.
723 <https://doi.org/10.1016/j.csr.2011.10.012>.

724 Lee TN, Atkinson LP (1983) Low-frequency current and temperature variability from gulf-
725 stream frontal eddies and atmospheric forcing along the southeast United States outer
726 continental-shelf. *J Geophys Res* 88(C8): 4541–4567.
727 <https://doi.org/10.1029/JC088iC08p04541>.

728 Matsuura H, Isoda Y, Kuroda H, Kuma K, Saitoh Y, Kobayashi N, Aiki T, Wagawa T, Yabe I,
729 Hoshiya Y (2007) Water mass modification process of the passage-flow waters through the
730 Tsugaru Strait. *Umi to Sora* 83:21–35 (in Japanese with English abstract).

731 Nishida Y, Kanomata I, Tanaka I, Sato S, Takahashi S, Matsubara H (2003) Seasonal and
732 Interannual Variations of the Volume transport through the Tsugaru Strait. *Oceanogr Jpn* 12:
733 487–499. <https://doi.org/10.5928/kaiyou.12.487> (in Japanese with English abstract).

734 Nof D, Pichevin T (2001) The Ballooning of Outflows. *J Phys Oceanogr* 31:3045–3058.
735 [https://doi.org/10.1175/1520-0485\(2001\)031<3045:TBOO>2.0.CO;2](https://doi.org/10.1175/1520-0485(2001)031<3045:TBOO>2.0.CO;2).

736 Ohshima K (1994) The flow system in the Japan Sea caused by a sea level difference through
737 shallow straits. *J Geophys Res* 99 (C5):9925-9940. <https://doi.org/10.1029/94JC00170>.

738 Ono H, Kosugi N, Toyama K, Tsujino H, Kojima A, Enyo K, Iida Y, Nakano T, Ishii M (2019)
739 Acceleration of ocean acidification in the Western North Pacific. *Geophys Res Lett* 46:13161–
740 13169. <https://doi.org/10.1029/2019GL085121>.

741 Onishi M, Ohtani K (1997) Volume transport of the Tsushima Warm Current, west of Tsugaru
742 Strait bifurcation area. *J Oceanogr* 53(1):27–34. <https://doi.org/10.1007/BF02700746>.

743 Onishi M, Isoda Y, Kuroda H, Iwahashi M, Satoh C, Nakayama T, Ito T, Iseda K, Nishizawa K,
744 Shima S, Togawa O (2004) Winter transport and tidal current in the Tsugaru Strait. *Bull Fish*
745 *Sci Hokkaido Univ.* 55, 105–119.

746 Pedlosky J (1987) *Geophysical Fluid Dynamics*, 2nd ed., Springer-Verlag, New York.

747 Pond S, Pickard G (1986) *Introductory Dynamical Oceanography*, 2nd ed., Elsevier, New York.

748 Qiu B, Toda T, Imasato N (1990) On Kuroshio front fluctuations in the East China Sea using
749 satellite and in situ observational data. *J Geophys Res* 95(C10):18,191–18,204.
750 <https://doi.org/10.1029/JC095iC10p18191>.

751 Rosa AL, Isoda Y, Uehara K, Aiki T (2007) Seasonal Variations of Water System Distribution
752 and Flow Patterns in the Southern Sea Area of Hokkaido, Japan. *J Oceanogr* 63:573–588.
753 <https://doi.org/10.1007/s10872-007-0051-4>.

754 Saitoh Y, Kuma K, Isoda Y, Kuroda H, Matsuura H, Wagawa T, Takata H, Kobayashi N, Nagano
755 S, Nakatsuka T (2008) Processes Influencing Iron Distribution in the Coastal Waters of the

756 Tsugaru Strait, Japan. *J Oceanogr* 64:815–830. <https://doi.org/10.1007/s10872-008-0068-3>.

757 Sato Y (1974) Environmental Factors Affecting to the Distribution of the Mackerel Shoals in
758 the Doto and the Sanriku Fishing Grounds, Northern Sea of Japan (1) Surface Water
759 Temperatures at the Fishing Spots. *Bull Tohoku Reg Fish Res Lab* 34:17–30 (in Japanese with
760 English abstract)

761 Schaeffer A, Gramouille A, Roughan M, Mantovanelli A (2017) Characterizing frontal eddies
762 along the East Australian Current from HF radar observations. *J Geophys Res* 122:3964–3980.
763 <https://doi.org/10.1002/2016JC012171>.

764 Sugimoto T, Kawasaki Y (1984) Seasonal and year-to-year variations of the Tsugaru Warm
765 Current and their dynamical interpretation. *Bull Coastal Oceanogr* 22:1–11 (in Japanese).

766 Sugimoto T, Kimura S, Miyaji K (1988) Meander of the Kuroshio front and current variability
767 in the East China Sea. *J Oceanogr Soc Jpn* 44:125–135. <https://doi.org/10.1007/BF02302619>.

768 Tanaka T, Hasegawa D, Okunishi T, Kaneko H, Ono T (2021) Internal Hydraulic Jump in the
769 Tsugaru Strait. *J Oceanogr*. <https://doi.org/10.1007/s10872-020-00588-w>.

770 Tanno T, Kuroda H, Isoda Y, Aiki T (2005) Flow Variations off Cape of Esan, northeast of
771 Tsugaru Strait. *Bull Fish Sci Hokkaido Univ* 562:33–41. (in Japanese with English abstract)

772 UNESCO (1983) Algorithms for computation of fundamental properties of seawater, 1983.
773 UNESCO Tech Pap in Mar Sci 44, 53pp.

774 Wagawa T, Kuroda H, Ito S, Kakehi S, Yamanome T, Tanaka K, Endoh Y, Kaga S (2015)
775 Variability in water properties and predictability of sea surface temperature along Sanriku coast,
776 Japan. *Cont Shelf Res* 103:12–22. <https://doi.org/10.1016/j.csr.2015.04.016>.

777 Wakita M, Nagano A, Fujiki T, Watanabe S (2017) Slow acidification of the winter mixed layer
778 in the subarctic western North Pacific. *J Geophys Res Oceans* 122:6923–6935.
779 <https://doi.org/10.1002/2017JC013002>.

780 Wakita M, Sasaki K, Nagano A, Abe H, Tanaka T, Nagano K, Sugie K, Kaneko H, Kimoto K,
781 Okunishi T, Takada M, Yoshino J, Watanabe S (2021) Rapid reduction of pH and CaCO₃
782 saturation state in the Tsugaru Strait by the intensified Tsugaru Warm Current during 2012-
783 2019, *Geophys Res Lett*. <https://doi.org/10.1029/2020GL091332>.

784 Yamaguchi T, Isoda Y, Itoh U, Mukai T, Kobayashi N (2020) Observation and model
785 experiments on an internal-wave packet accompanied by streak bands over the sill topography
786 of Tsugaru Strait. *Oceanogr Jpn* 29, 71–90. https://doi.org/10.5928/kaiyou.29.3_71. (in
787 Japanese with English abstract)

788 Yanagi T, Shimizu T, Lie HJ (1998) Detailed structure of the Kuroshio frontal eddy along the
789 shelf edge of the East China Sea. *Cont Shelf Res* 18: 1039–1056.
790 [https://doi.org/10.1016/S0278-4343\(98\)80005-8](https://doi.org/10.1016/S0278-4343(98)80005-8).

791 Yasuda I, Okuda K, Hirai M, Ogawa Y, Kudoh H, Fukushima S, Mizuno K (1988) Short-Term

792 Variations of the Tsugaru Warm Current in Autumn. Bull Tohoku Reg Fish Res Lab 50:153–
793 191 (in Japanese with English abstract)

794 Yoshikawa Y, Masuda A, Marubayashi K, Ishibashi M, Okuno A (2006) On the accuracy of HF
795 radar measurement in the Tsushima Strait. J Geophys Res 111:C04009,
796 <https://doi.org/10.1029/2005JC003232>.

797 Yoshikawa Y, Masuda A, Marubayashi K, Ishibashi M (2010) Seasonal variations of the surface
798 currents in the Tsushima Strait. J Oceanogr 66:223–232. [https://doi.org/10.1007/s10872-010-](https://doi.org/10.1007/s10872-010-0020-1)
799 [0020-1](https://doi.org/10.1007/s10872-010-0020-1).

800

801

802 **Figure legends**

803 Figure 1. (a) Schematic diagram of the flows around Japan. (b) Locations of stations along the
804 repeated observation lines around the Tsugaru Strait. (c) Observation site of the present study
805 and distribution of the temporal mean velocity at each grid point for 2017–2019. Contours in
806 (b) denote topography. The square grids in (c) indicate the bins used to calculate the zonal
807 average of the zonal velocity.

808 Figure 2. Mean latitude of the axis of the TWC (squares) with standard deviation (blue lines) at
809 each grid in each season of (a) winter, (b) spring, (c) summer, and (d) autumn. Colors of the

810 squares denote mean value of the zonal velocity at the axis. Contours and triangles are same
811 with those in Fig. 1.

812 Figure 3. Standard deviation of the axis of the TWC calculated using the bootstrap method
813 (thick lines) in each monthly of (a) winter, (b) spring, (c) summer, and (d) autumn. Thin lines
814 indicate 95 % confidence interval of the bootstrap method. Broken lines correspond to the
815 location of the Shiriya Spur.

816 Figure 4. Examples of short-variation of the axis of the TWC. Each-one-day-mean of the
817 latitude of the axis of the TWC is shown. The upper row labeled as (a) is that in August in 2017.
818 The lower row labeled as (b) is that in February in 2018. Contours and triangles are same with
819 those in Fig. 1.

820 Figure 5. Power spectral density (PSD) of the latitude of the TWC's axis calculated from data
821 for 2018–2019 in each sub-region of (a) R1–R12, and (b) R13–25. Lat, and CPD mean the
822 degree of latitude, and cycle per day, respectively. For ease of viewing, each data is displayed
823 with slightly shift of increments in the vertical axis direction. Thin solid lines denote 95 %
824 confidence interval. Dark (light) gray broken line denotes the timescale of 13.66 (27.32) days.

825 Figure 6. Examples of lag-correlation (r) of some sub-regions in relation to the reference sub-
826 region (R1) in 2017. Triangles show peaks of the lag correlation. Thin lines denote 95 %
827 confidence interval.

828 Figure 7. Distance–lag plot in each season; (a) spring, (b) summer, (c) autumn, and (d) winter.
829 Plots with dark(light)-gray-color denote the first (second) cycle of the propagation starting from
830 the lag 0 (13.7) days. Thin (thick) solid line denotes the propagation speed estimated from the
831 Eq. 4 (based on Eady’s theory). Broken lines indicate advection time-scale of the upper- and
832 lower-layer. Vertical solid (broken) lines denote the corresponding location of the Shiriya Spur
833 (Shiriya–Esan-line).

834 Figure 8. Vertical transection of seasonal mean of the salinity (color), and potential density
835 anomaly, σ_θ (contour), along the Shiriya–Esan-line in (a) spring, (b) summer, (c) autumn, and
836 (d) winter. Triangles show the latitude of each station. Circle with error bar is a position of the
837 TWC axis for 2017–2019 with standard deviation. Broken magenta line denotes the depth of
838 the upper-layer, H_1 .

839 Figure 9. As Fig. 8, but for the geostrophic velocity across the Shiriya–Esan-line (outflow from
840 the strait is positive). (a) spring, (b) summer, (c) autumn, and (d) winter.

841 Figure 10. Typical vertical structure in each season of (a) potential density anomaly, σ_θ , and (b)
842 zonal velocity in the Esan–Shiriya-line. Note that whereas (a) is the seasonal isodepth mean of
843 σ_θ , from the station SE3 to SE7, (b) is the seasonal isodepth mean of the geostrophic velocity
844 for the stations SE3–SE7 (as an exception, SE4–SE6 in winter). Triangles are the upper-layer
845 depth, H_1 , in each season.

846

847 Fig. S1. Example of low-pass-filtered timeseries of the latitude of the TWC's axis in 2017,
848 using the fifth-order butterworth filter that has the cutoff timescale of 10 days.

849

850

851

852

853

854

855

856

857

858

859

860

861

862

863 **Tables**

864 Table 1. Locations of the stations of the repeated shipboard observations.

Station	Latitude (°N)	Longitude (°E)
SE1	41.44	141.42
SE2	41.48	141.40
SE3	41.53	141.37
SE4	41.58	141.35
SE5	41.64	141.32
SE6	41.68	141.30
SE7	41.74	141.26
SE8	41.79	141.25
SE9	41.83	141.22

865

866

867

868

869

870

871

872

873

874 Table 2. Implementation record of hydrographic observations along the Shiriya–Esan (SE) line.

875 The character of U, O, and W represent the observations conducted by T/S *Ushio-Maru*, T/S

876 *Oshoro-Maru*, and R/V *Wakataka-Maru*, respectively.

877

Year	Winter			Spring			Summer			Autumn		
	Jan.	Feb.	Mar.	Apr.	May	Jun.	Jul.	Aug.	Sep.	Oct.	Nov.	Dec.
2009											U	
2010		U			U			U			U	
2011		O			U		U				U	
2012		U				U		U			U	
2013					U			U				
2014		U			U			U			U	
2015		U	U		U						U	
2016		U			U	U					U	
2017					U							
2018		U						W				
2019				U					W		U	

878

Figures

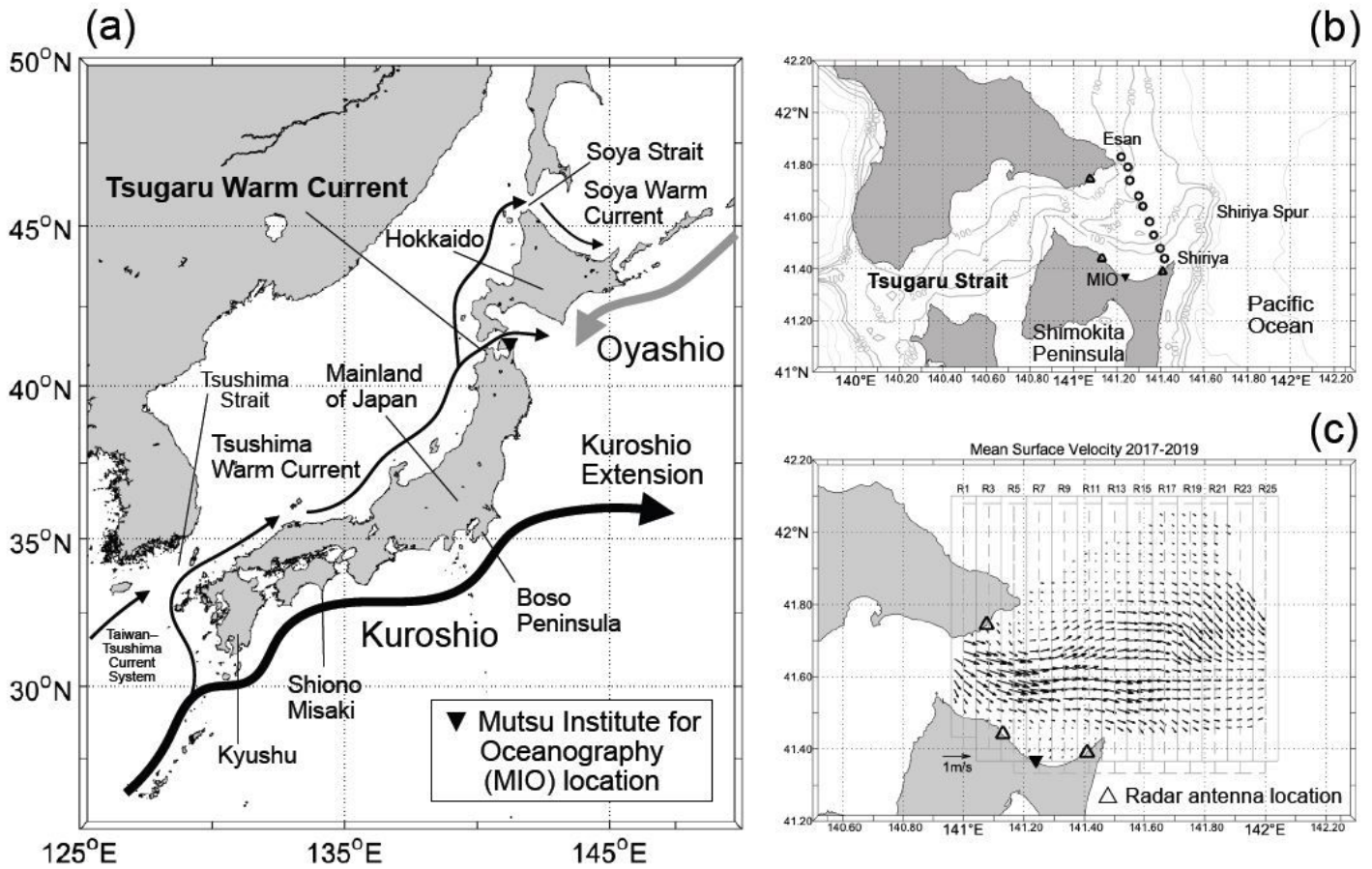


Figure 1

(a) Schematic diagram of the flows around Japan. (b) Locations of stations along the repeated observation lines around the Tsugaru Strait. (c) Observation site of the present study and distribution of the temporal mean velocity at each grid point for 2017–2019. Contours in (b) denote topography. The square grids in (c) indicate the bins used to calculate the zonal average of the zonal velocity.

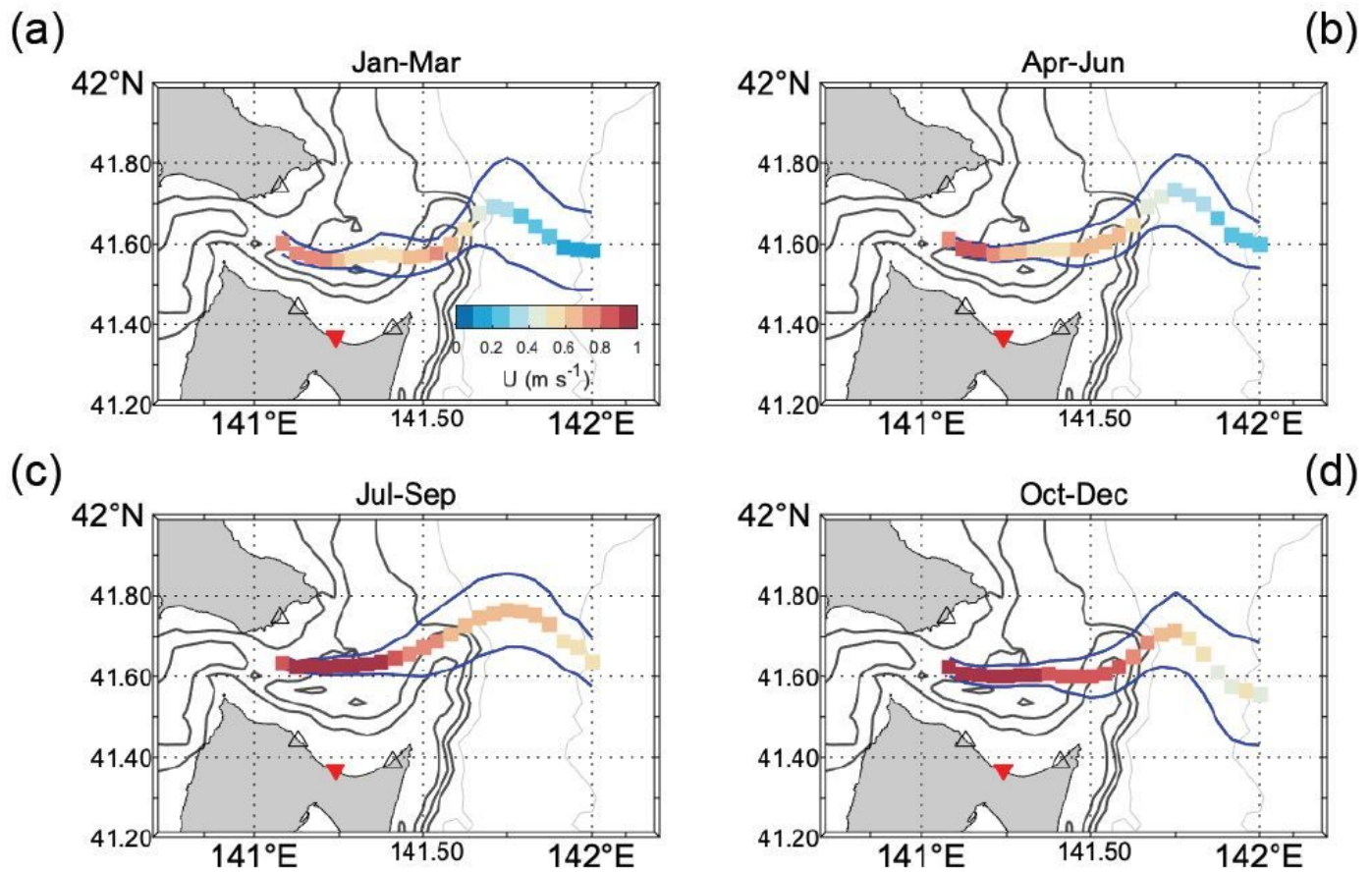


Figure 2

Mean latitude of the axis of the TWC (squares) with standard deviation (blue lines) at each grid in each season of (a) winter, (b) spring, (c) summer, and (d) autumn. Colors of the squares denote mean value of the zonal velocity at the axis. Contours and triangles are same with those in Fig. 1.

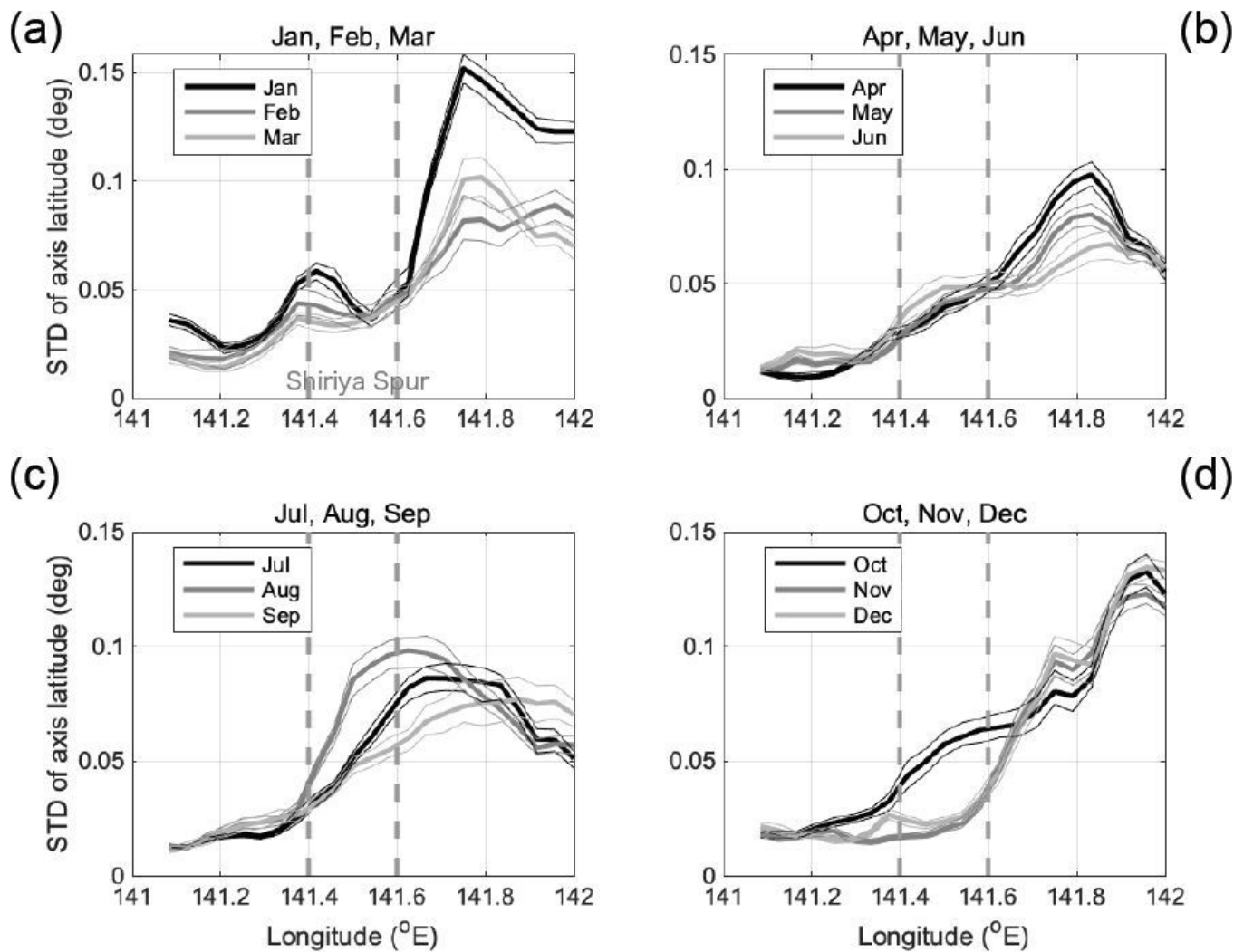


Figure 3

Standard deviation of the axis of the TWC calculated using the bootstrap method (thick lines) in each monthly of (a) winter, (b) spring, (c) summer, and (d) autumn. Thin lines indicate 95 % confidence interval of the bootstrap method. Broken lines correspond to the location of the Shiriya Spur.

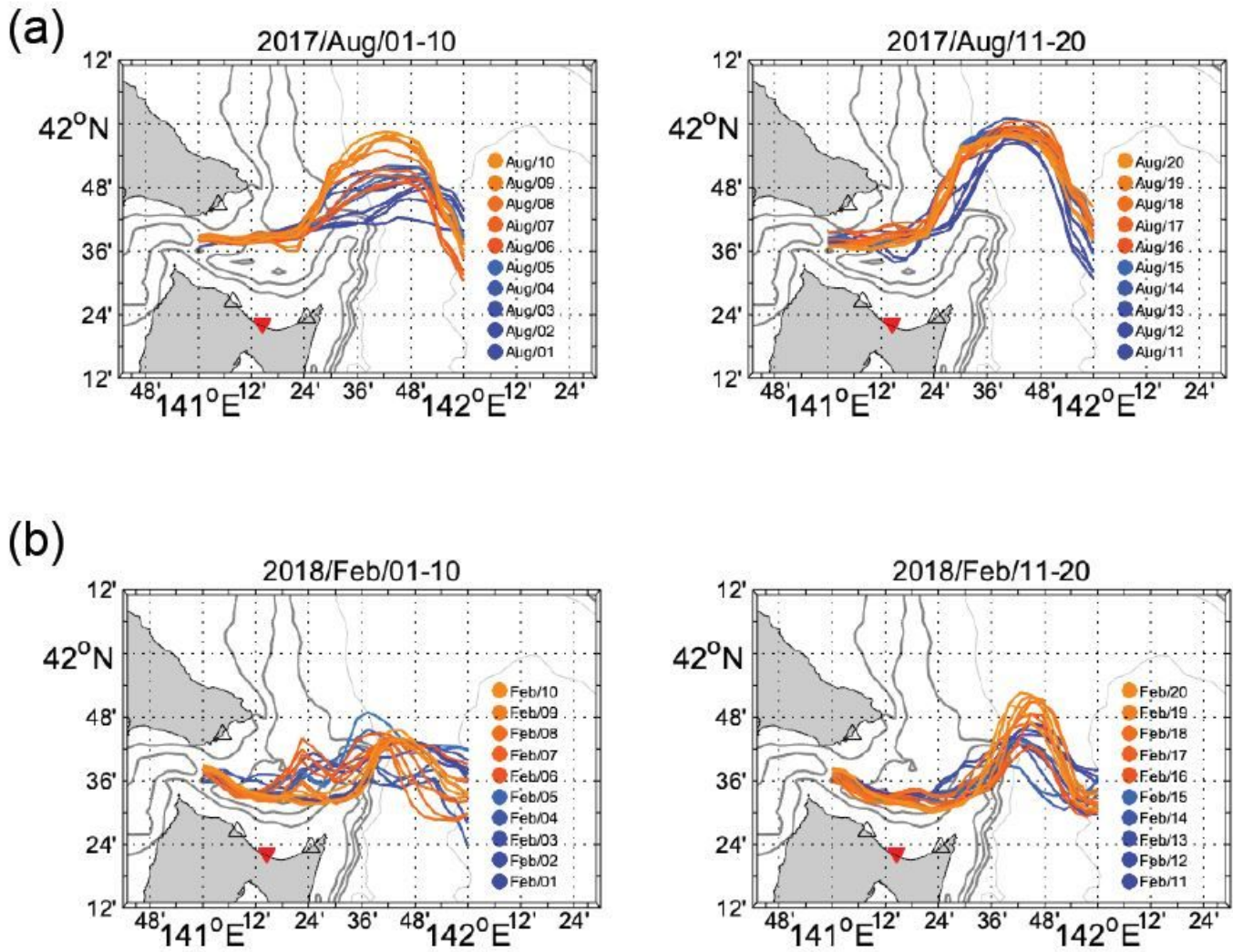


Figure 4

Examples of short-variation of the axis of the TWC. Each-one-day-mean of the latitude of the axis of the TWC is shown. The upper row labeled as (a) is that in August in 2017. The lower row labeled as (b) is that in February in 2018. Contours and triangles are same with those in Fig. 1.

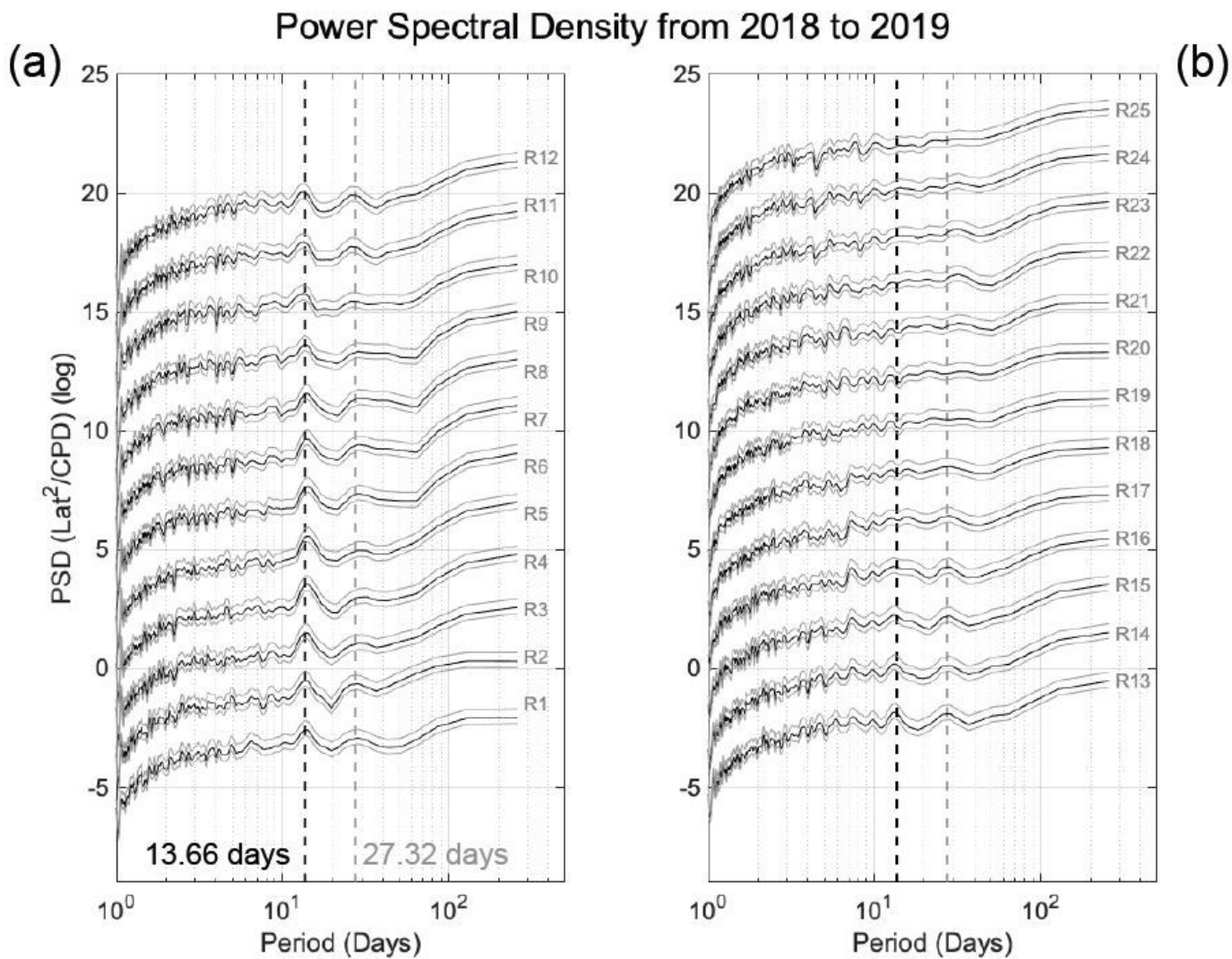


Figure 5

Power spectral density (PSD) of the latitude of the TWC's axis calculated from data for 2018–2019 in each sub-region of (a) R1–R12, and (b) R13–25. Lat, and CPD mean the degree of latitude, and cycle per day, respectively. For ease of viewing, each data is displayed with slightly shift of increments in the vertical axis direction. Thin solid lines denote 95 % confidence interval. Dark (light) gray broken line denotes the timescale of 13.66 (27.32) days.

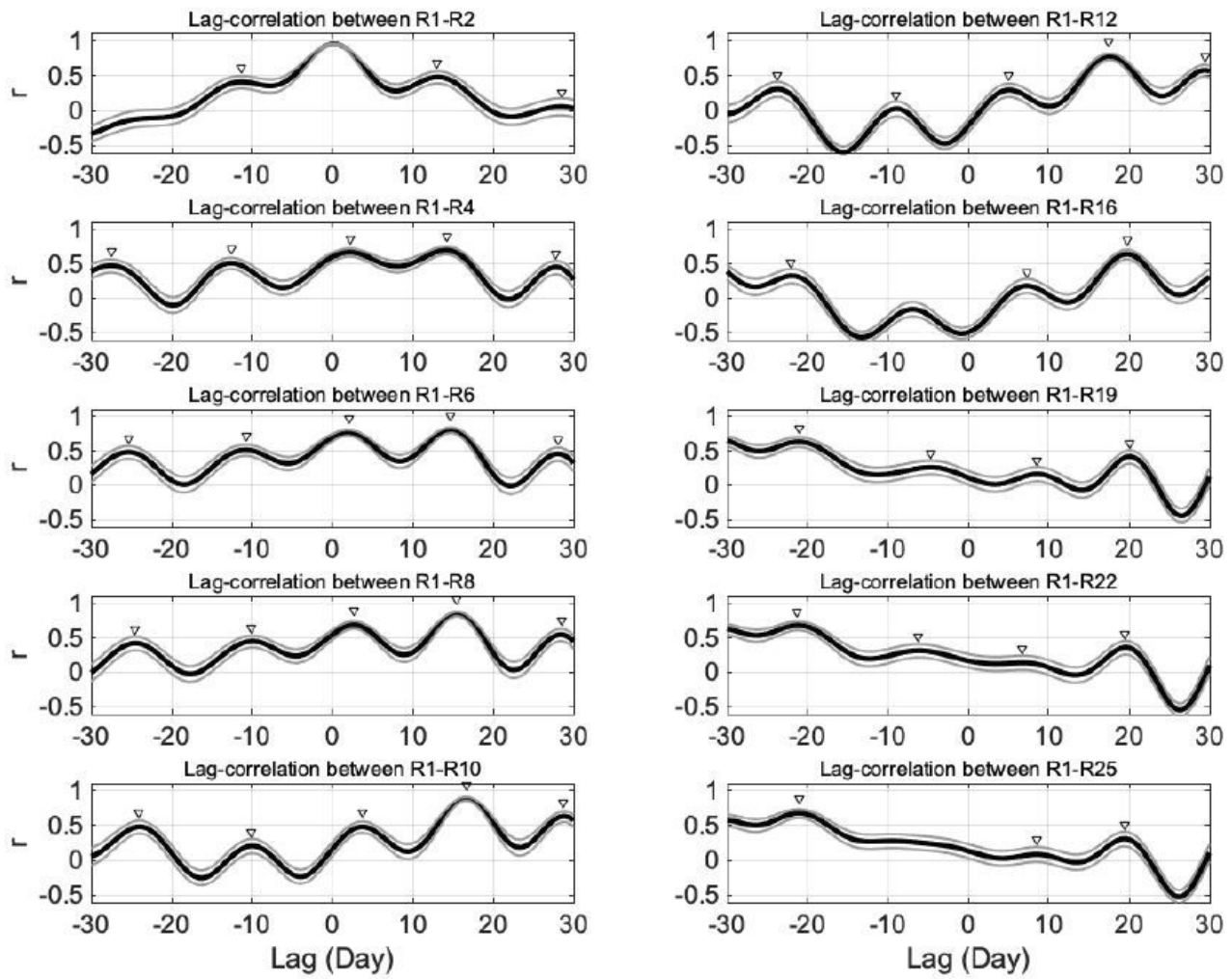


Figure 6

Examples of lag-correlation (r) of some sub-regions in relation to the reference sub-region (R1) in 2017. Triangles show peaks of the lag correlation. Thin lines denote 95 % confidence interval.

Propagation Speed compared with SE-line U_{GV}

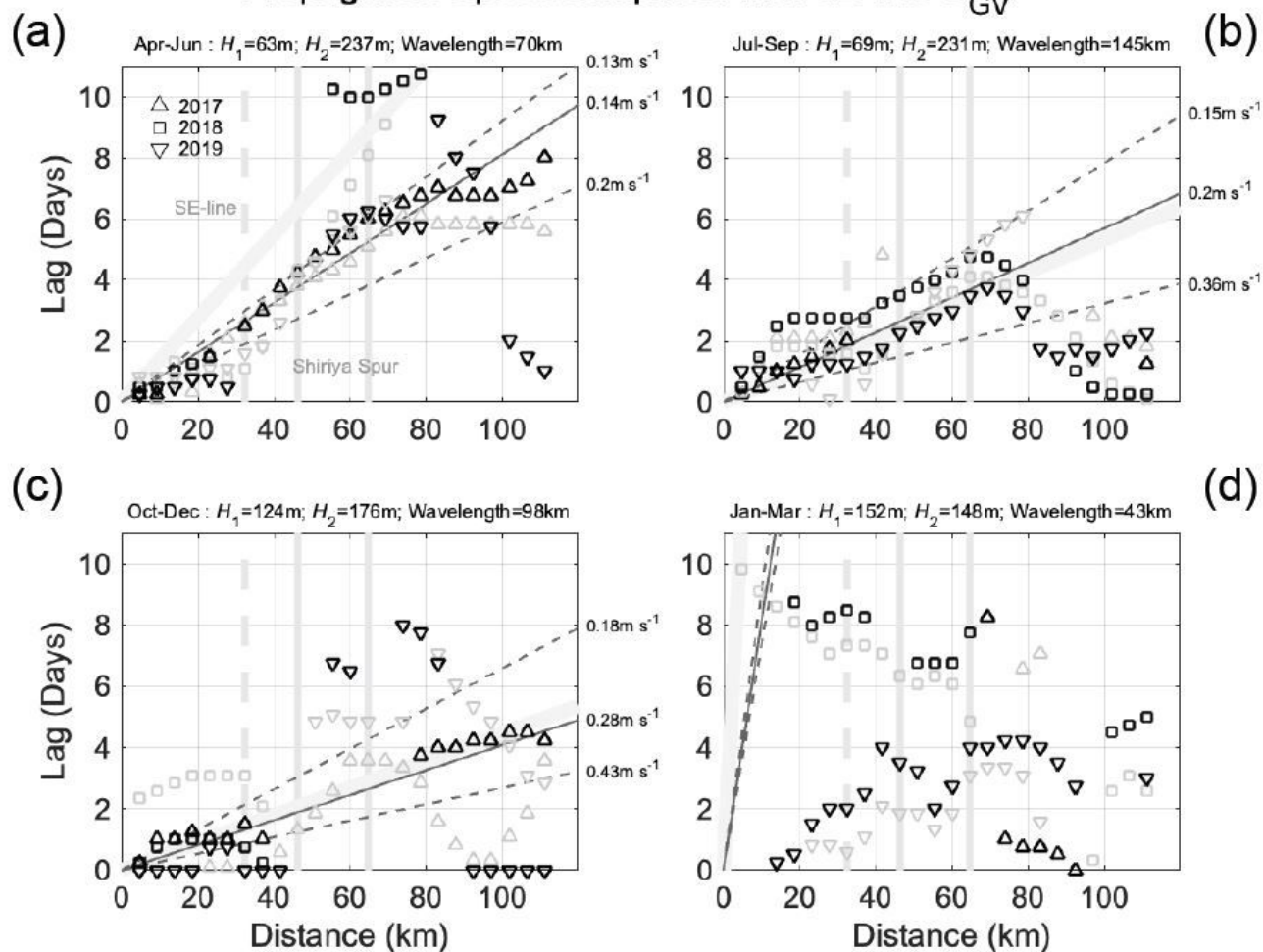


Figure 7

Distance–lag plot in each season; (a) spring, (b) summer, (c) autumn, and (d) winter. Plots with dark(light)-gray-color denote the first (second) cycle of the propagation starting from the lag 0 (13.7) days. Thin (thick) solid line denotes the propagation speed estimated from the Eq. 4 (based on Eady's theory). Broken lines indicate advection time-scale of the upper- and lower-layer. Vertical solid (broken) lines denote the corresponding location of the Shiriya Spur (Shiriya–Esan-line).

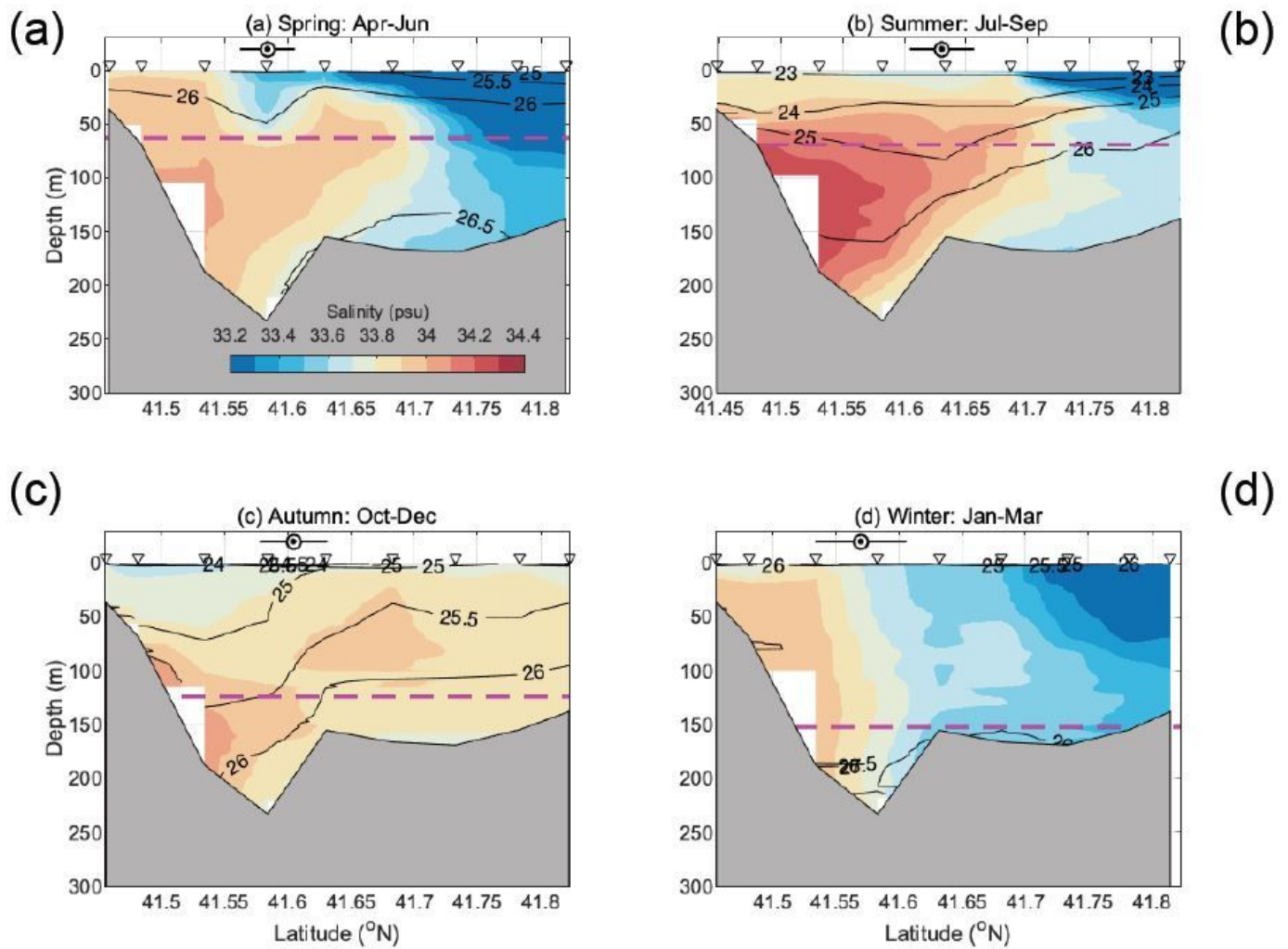


Figure 8

Vertical transection of seasonal mean of the salinity (color), and potential density anomaly, σ_{θ} (contour), along the Shiriya-Esan-line in (a) spring, (b) summer, (c) autumn, and (d) winter. Triangles show the latitude of each station. Circle with error bar is a position of the TWC axis for 2017-2019 with standard deviation. Broken magenta line denotes the depth of the upper-layer, H1.

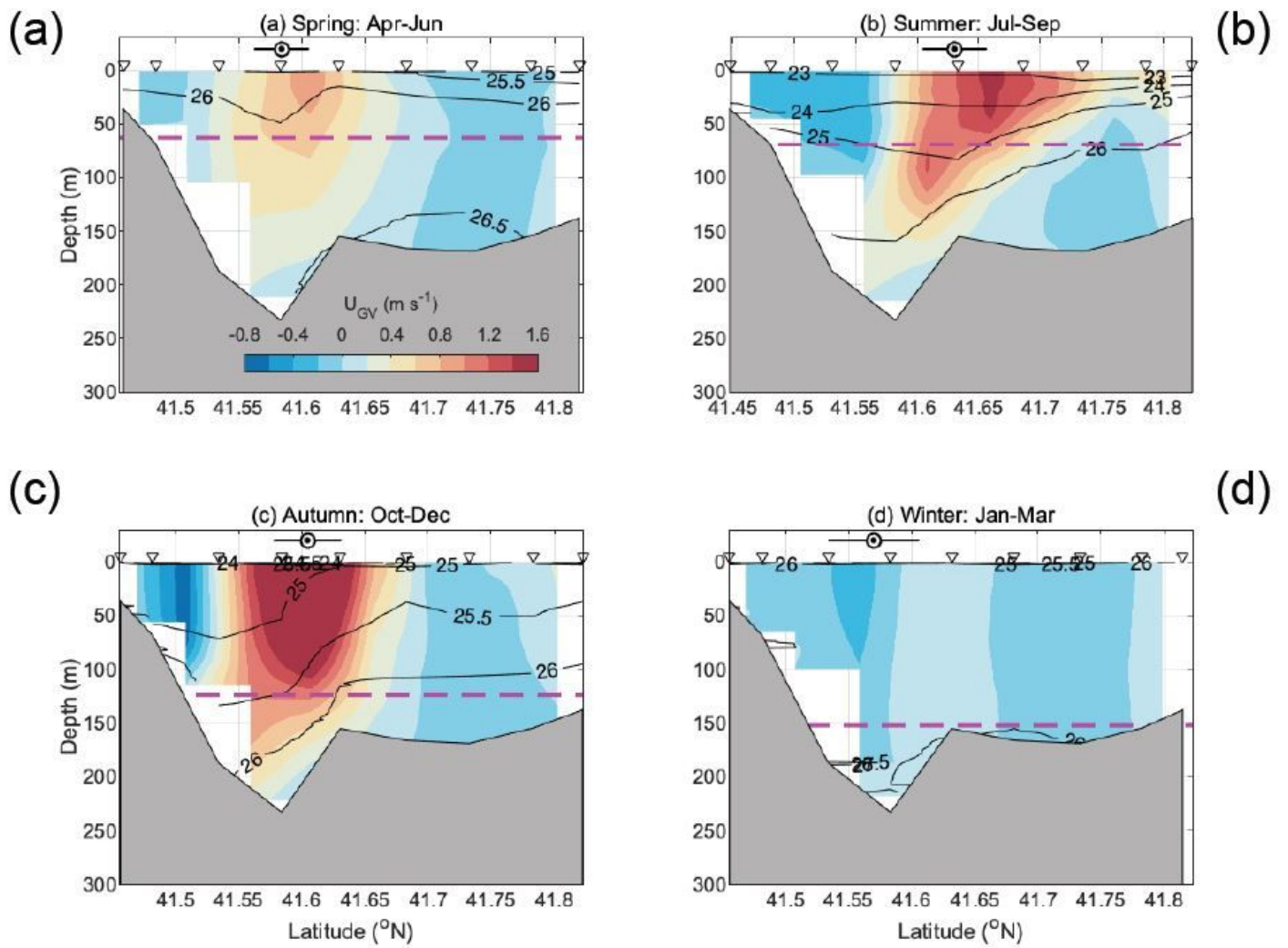


Figure 9

As Fig. 8, but for the geostrophic velocity across the Shiriya–Esan-line (outflow from the strait is positive). (a) spring, (b) summer, (c) autumn, and (d) winter.

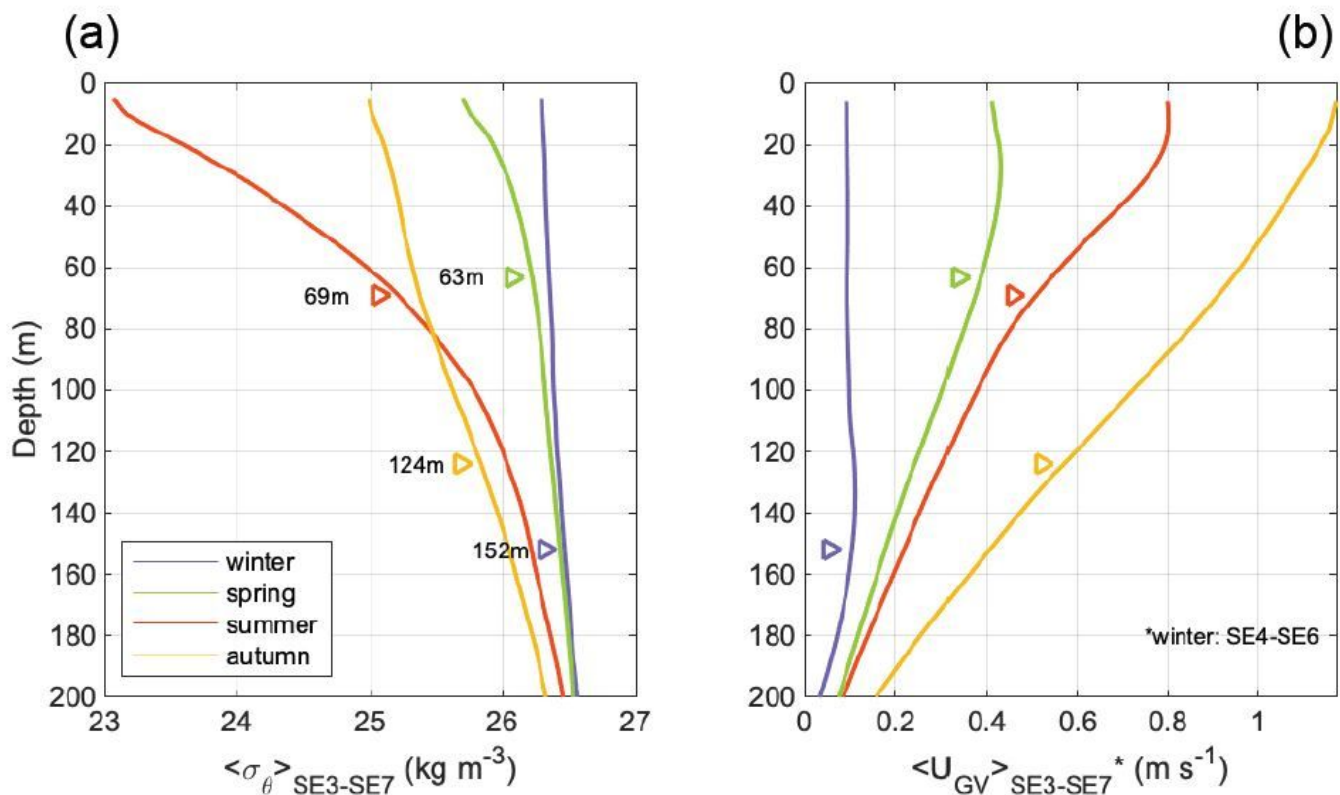


Figure 10

Typical vertical structure in each season of (a) potential density anomaly, σ_θ , and (b) zonal velocity in the Esan–Shiriyu-line. Note that whereas (a) is the seasonal isodepth mean of σ_θ , from the station SE3 to SE7, (b) is the seasonal isodepth mean of the geostrophic velocity for the stations SE3–SE7 (as an exception, SE4–SE6 in winter). Triangles are the upper-layer depth, H1, in each season.

Supplementary Files

This is a list of supplementary files associated with this preprint. Click to download.

- [SuppFig1.jpg](#)